Validation of Large-Eddy Simulation Methods for Gravity-Wave Breaking

Sebastian Remmler* and Stefan Hickel† ‡

Institute of Aerodynamics and Fluid Mechanics, Technische Universität München, Germany.

Mark D. Fruman and Ulrich Achatz

Institute for Atmosphere and Environment, Goethe-University Frankfurt, Germany.

*Current affiliation: AUDI AG, I/EK-44, 85045 Ingolstadt, Germany.

†Current affiliation: Delft University of Technology, The Netherlands.

‡*Corresponding author address:* Stefan Hickel, Department of Aerospace Engineering, Delft University of Technology, Kluyverweg 1, 2629 HS Delft, The Netherlands.

E-mail: sh@tum.de

ABSTRACT

In order to reduce the computational costs of numerical studies of gravity wave breaking in the atmosphere, the grid resolution has to be reduced as much as possible. Insufficient resolution of small-scale turbulence demands a proper turbulence parametrisation in the framework of large-eddy simulation (LES). We validate three different LES methods – the Adaptive Local Deconvolution Method (ALDM), the dynamic Smagorinsky method (DSM) and a naïve central discretisation without turbulence parametrisation (CDS4) – for three different cases of the breaking of well defined monochromatic gravity waves. For ALDM we developed a modification of the numerical flux functions that significantly improves the simulation results in case of a temporarily very smooth velocity field. The test cases include an unstable and a stable inertia-gravity wave as well as an unstable high-frequency gravity wave. All simulations are carried out both in three-dimensional domains and in two-dimensional domains in which the velocity and vorticity fields are three dimensional (so-called 2.5-D simulations). We find that results obtained with ALDM and DSM are generally in good agreement with the reference direct numerical simulations as long as the resolution in the direction of the wave vector is sufficiently high. The resolution in the other directions has a weaker influence on the results. The simulations without turbulence parametrisation are only successful if the resolution is high and the level of turbulence comparatively low.

1. Introduction

Gravity waves are a common phenomenon in any stably stratified fluid, such as the atmosphere of the earth. They can be excited by flow over orography (e.g. Smith 1979; McFarlane 1987), by convection (e.g. Chun et al. 2001; Grimsdell et al. 2010), and by spontaneous imbalance of the mean flow in the troposphere (O'Sullivan and Dunkerton 1995; Plougonven and Snyder 2007). Gravity waves transport energy and momentum from the region where they are forced to the region where they are dissipated (e.g. through breaking), possibly far away from the source region. Various phenomena, such as the cold summer mesopause (Hines 1965) and the quasi-biennial oscillation in the equatorial stratosphere (e.g. Baldwin et al. 2001), cannot be explained nor reproduced in weather and climate simulations without accounting for the effect of gravity waves. See Fritts and Alexander (2003) for an overview of gravity waves in the middle atmosphere. Prusa et al. (1996) found in numerical experiments that (due to wave dispersion) gravity waves generated in the troposphere at a broad wavelength spectrum reach the upper mesosphere as an almost monochromatic wave packet with a horizontal wavelength between a few kilometres and more than 100 km, depending on the horizontal scale of the forcing and the background conditions.

Since most gravity waves have a wavelength that is not well resolved in general circulation models, the effect of gravity waves on the global circulation is usually accounted for by parametrisation based on combinations of linear wave theory (Lindzen 1981), empirical observations of time-mean energy spectra (e.g. Hines 1997), and simplified treatments of the breaking process. See Kim et al. (2003) and McLandress (1998) for reviews of the various standard parametrisation schemes.

A common weakness of most parametrisation schemes is the over-simplified treatment of the wave breaking process. Improving this point requires a deeper insight into the breaking process that involves generation of small scale flow features through wave-wave interactions and through

wave-turbulence interactions. Since the gravity-wave wavelength and the turbulence that eventually leads to energy dissipation into heat span a wide range of spatial and temporal scales, the breaking process is challenging both for observations and numerical simulations. Direct Numerical Simulations (DNS) must cover the breaking wave with a wavelength of a few kilometres as well as the smallest turbulence scales (the Kolmogorov length η). The Kolmogorov length depends on the kinetic energy dissipation and the kinematic viscosity. It is on the order of millimetres in the troposphere (Vallis 2006) and approximately 1 m at 80 km altitude (Remmler et al. 2013).

The necessity of resolving the Kolmogorov scale can be circumvented by applying the approach of Large-Eddy Simulation (LES), i.e. by parametrising the effect of unresolved small eddies on the resolved large-scale flow.

This can be necessary in cases where DNS would be too expensive, e.g. in investigating the dependence of the gravity wave breaking on several parameters (propagation angle, wavelength, amplitude, viscosity, stratification) at the same time; for problems in which many wavelengths need to be resolved – such as propagation of a wave packet or wave train through a variable background (Lund and Fritts 2012) or modelling realistic cases of waves generated by topography or convection; for validating quasilinear wave-propagation theory (Muraschko et al. 2014); or for validating gravity-wave-drag parametrisation schemes.

The subgrid-scale parametrisation of turbulence is, of course, a source of uncertainty and, where possible, should be validated against fully resolved DNS or observations for every type of flow for which it is to be used. Many numerical studies of breaking gravity waves rely on the LES principle without such a validation (e.g. Winters and D'Asaro 1994; Lelong and Dunkerton 1998; Andreassen et al. 1998; Dörnbrack 1998; Afanasyev and Peltier 2001).

Recent studies (Fritts et al. 2009, 2013; Fritts and Wang 2013) have presented highly resolved, high Reynolds number DNS of a monochromatic gravity wave breaking. However, they do not

take into account the Coriolis force, which has a large influence on the dynamics of breaking for low-frequency gravity waves (Dunkerton 1997; Achatz and Schmitz 2006b), often referred to as inertia-gravity waves (IGWs) as opposed to high-frequency gravity waves (HGWs). The Coriolis force induces an elliptically polarised transverse velocity field in IGWs, and the velocity component normal to the plane of propagation of the wave has its maximum shear at the level of minimum static stability. Dunkerton (1997) and Achatz and Schmitz (2006b) showed that this strongly influences the orientation of the most unstable perturbations.

An important aspect in setting up a simulation of a gravity wave breaking event is the proper choice of the domain size and initial conditions. While the gravity wave itself depends on one spatial coordinate and has a natural length scale given by its wavelength, the breaking process and the resulting turbulence is three-dimensional and proper choices have to be made for the domain sizes in the two directions perpendicular to the wave vector. Achatz (2005) and Achatz and Schmitz (2006a) analysed the primary instabilities of monochromatic gravity waves of various amplitudes and propagation directions using normal-mode and singular-vector analysis, and Fruman and Achatz (2012) extended this analysis for IGWs by computing the leading secondary singular vectors with respect to a time-dependent simulation of the perturbed wave. (Normal-mode analysis is not suited to time-dependent basic states, while singular-vector analysis, whereby the perturbations whose energy grows by the largest factor in a given optimisation time, is always possible.) They found that the wavelength of the optimal secondary perturbation can be much shorter than the wavelength of the original wave. Thus the computational domain for a three-dimensional simulation need not necessarily have the size of the base wavelength in all three directions. They proposed the following multi-step approach to set-up the domain and initial conditions for a DNS of a given monochromatic gravity wave:

1. solution (in the form of normal modes or singular vectors) of the governing (Boussinesq) equations linearised about the basic state wave, determining the primary instability structures;

2. two-dimensional (in space) numerical solution of the full nonlinear equations using the result of stage 1 as initial condition;

3. solution in the form of singular vectors (varying in the remaining spatial direction) of the governing equations linearised about the time-dependent result of stage 2;

4. three-dimensional DNS using the linear solutions from stages 1 and 3 as initial condition and their wavelengths for the size of the computational domain.

This procedure was applied to an unstable IGW by Remmler et al. (2013) and fully elaborated with two additional test cases by Fruman et al. (2014).

Having these properly designed DNS results available, we can now use them for the validation of computationally less expensive methods. Hence the present study analyses the suitability of different LES methods for the cases presented by Fruman et al. (2014), viz. an unstable IGW, a stable IGW and an unstable HGW, all of them with a base wavelength of 3 km. The first LES method to be applied is the Adaptive Local Deconvolution Method (ALDM) of Hickel et al. (2006, 2014). It is an "implicit" LES method since the SGS stress parametrisation is implied in the numerical discretisation scheme. Based on ALDM for incompressible flows and its extension to passive scalar mixing (Hickel et al. 2008), Remmler and Hickel (2012, 2013); Rieper et al. (2013) successfully applied ALDM to stably stratified turbulent flows.

For the present study, the numerical flux function for the active scalar in ALDM has been modified to prevent the method from generating spurious oscillations in partially laminar flow fields.

The second method to be applied is the the well known Smagorinsky (1963) method with the dynamic estimation of the spatially nonuniform model parameter proposed by Germano et al.

(1991) and refined by Lilly (1992). The third LES method is a "naïve" approach with a simple central discretisation scheme and no explicit SGS parametrisation. This method is theoretically dissipation-free but can lead to numerical instability if the turbulence level is high (which was the reason for the development of the first explicit SGS parametrisation by Smagorinsky 1963). However, the method is computationally inexpensive and can be used in some cases without problems, as we will show.

We apply these methods to the three gravity-wave test cases using grids of different refinement levels with the goal of using as few grid cells as possible while still obtaining good agreement with the DNS results. We also run small ensembles for each simulation with only slightly different initial conditions to get an estimate of the sensitivity and variability of the results. All this is done in a three dimensional domain (with the same domain size as the DNS) and in a two-dimensional domain in which the two dimensions are chosen to be parallel to the wave vectors of the gravity wave and of the most important growing primary perturbation (without the addition of the secondary singular vector, cf. step 2 above). Since the velocity and vorticity fields are three-dimensional and since the turbulent cascade is *direct* (energy moves to smaller length scales), these simulations are sometimes called "2.5-D". Fruman et al. (2014) found that 2.5-D and 3-D results are broadly very similar for the inertia–gravity-wave test cases considered here.

The paper is organised as follows. In section 2 the governing equations used for the simulations are presented along with properties of the inertia-gravity wave solutions and the energetics of the system. Section 3 describes the numerical methods used, in particular the three LES schemes. The three test cases are reviewed in section 4 and the results of the simulations are discussed in sections 5 to 7.

2. Governing equations

Assuming the vertical wavelength of the inertia-gravity wave is small compared to the density scale-height of the atmosphere, the dynamics are reasonably well approximated by the Boussinesq equations on an f plane. For mathematical convenience we further assume that the molecular viscosity and diffusion as well as the Brunt-Väisälä frequency of the background are constants, independent of space and time.

Since there is no preferred horizontal direction on an f plane, there is no loss of generality in assuming the basic wave propagates in the (y,z)-plane. In all three test cases, the primary perturbation is *transverse* (corresponding to an angle of $\alpha = 90^\circ$ in the nomenclature of Fruman et al. (2014)). It is thus advantageous to rotate the coordinate system with respect to the earth coordinates (x,y,z) through an angle $90^\circ - \Theta$ about the x axis (where Θ is the angle the wavevector makes with the y axis) such that one coordinate direction is parallel to the wave vector. We thus define the rotated Cartesian coordinates

$$x_\parallel = x, \tag{1a}$$

$$y_\perp = z\cos\Theta + y\sin\Theta, \tag{1b}$$

$$\zeta = z\sin\Theta - y\cos\Theta, \tag{1c}$$

and the corresponding velocity vector $\boldsymbol{u} = \left(u_\parallel, v_\perp, w_\zeta\right)$. The rotated coordinate system is sketched in fig. 1.

The Boussinesq equations on an f plane are, in vector form,

$$\nabla\cdot\boldsymbol{u} = 0, \tag{2a}$$

$$\partial_t\boldsymbol{u} + (\boldsymbol{u}\cdot\nabla)\,\boldsymbol{u} = -f\hat{\boldsymbol{e}}_z\times\boldsymbol{u} + b\hat{\boldsymbol{e}}_z - \nabla p + \nu\nabla^2\boldsymbol{u} + \mathscr{F}, \tag{2b}$$

$$\partial_t b + (\boldsymbol{u}\cdot\nabla)\,b = -N^2\hat{\boldsymbol{e}}_z\cdot\boldsymbol{u} + \mu\nabla^2 b + \mathscr{B}, \tag{2c}$$

where b is buoyancy, p is pressure normalised by a constant background density, and $\hat{\boldsymbol{e}}_z = (0, \sin\Theta, \cos\Theta)$ is the unit vector in the true vertical direction. N is the constant Brunt-Väisälä frequency, f is the Coriolis parameter, ν and μ are the kinematic viscosity and thermal diffusivity, respectively, and $\mathscr{F}$ and $\mathscr{B}$ represent the influence of an explicit turbulence SGS parametrisation.

An inertia-gravity wave, propagating at an angle Θ with respect to the horizontal plane is a solution to (2) of the form

$$\begin{bmatrix} u_\parallel \\ v_\perp \\ w_\zeta \\ b \end{bmatrix} = \Re\left\{ a \begin{bmatrix} \frac{f}{k} \\ -\frac{iK\omega}{km} \\ 0 \\ -\frac{N^2}{m} \end{bmatrix} e^{i\phi} \right\}, \tag{3}$$

where K is the magnitude of the wavevector, $k = K\cos\Theta$ and $m = K\sin\Theta$ are its horizontal and vertical components in the Earth frame, $\phi = K\zeta - \omega t$ is the wave phase and

$$\omega = -\sqrt{f^2\sin^2\Theta + N^2\cos^2\Theta} \tag{4}$$

is the wave frequency (the negative sign was chosen so that the wave has an upward group velocity). The non-dimensional (complex) wave amplitude a is defined such that a wave with $|a| = 1$ is neutral with respect to static instability at its least stable point. Waves with $|a| > 1$ are statically unstable and waves with $|a| < 1$ are statically stable. The phase velocity of the wave is directed in the negative ζ direction.

The local kinetic and available potential energy density in the flow are defined as

$$E_\mathrm{k} = \frac{1}{2}\boldsymbol{u}^\top\boldsymbol{u}, \qquad E_\mathrm{p} = \frac{b^2}{2N^2}, \tag{5}$$

with the total energy defined as the sum $E_\mathrm{t} = E_\mathrm{k} + E_\mathrm{p}$. We obtain the transport equations of the energy components by scalar-multiplying eq. (2b) by $\boldsymbol{u}$ and (2c) by b/N^2 and applying the

divergence constraint (2a):

$$\partial_t E_\mathrm{k} + \nabla\cdot(\boldsymbol{u}E_\mathrm{k}) = -f\boldsymbol{u}\cdot(\hat{\boldsymbol{e}}_z\times\boldsymbol{u}) - b\boldsymbol{u}\cdot\hat{\boldsymbol{e}}_z - \boldsymbol{u}\cdot\nabla p + \nu\left[\nabla^2 E_\mathrm{k} - (\nabla\boldsymbol{u})^2\right] + \boldsymbol{u}\cdot\mathscr{F}, \tag{6a}$$

$$\partial_t E_\mathrm{p} + \nabla\cdot\left(\boldsymbol{u}E_\mathrm{p}\right) = b\boldsymbol{u}\cdot\hat{\boldsymbol{e}}_z + \mu\left[\nabla^2 E_\mathrm{p} + \frac{(\nabla b)^2}{N^2}\right] + \frac{b\mathscr{B}}{N^2}. \tag{6b}$$

Based on these, we define the following contributions to the spatially averaged energy dissipation in an underresolved simulation as

$$\varepsilon_\mathrm{m} = \varepsilon_\mathrm{k,m} + \varepsilon_\mathrm{p,m} \tag{7a}$$

$$= \left\langle \nu\left[(\nabla\boldsymbol{u})^2 - \nabla^2 E_\mathrm{k}\right]\right\rangle_\mathrm{s} + \left\langle \mu\left[\frac{(\nabla b)^2}{N^2} - \nabla^2 E_\mathrm{p}\right]\right\rangle_\mathrm{s},$$

$$\varepsilon_\mathrm{s} = \varepsilon_\mathrm{k,s} + \varepsilon_\mathrm{p,s} = \langle\boldsymbol{u}\cdot\mathscr{F}\rangle_\mathrm{s} + \left\langle\frac{\boldsymbol{u}\cdot\mathscr{B}}{N^2}\right\rangle_\mathrm{s}, \tag{7b}$$

$$\varepsilon_\mathrm{n} = \varepsilon_\mathrm{k,n} + \varepsilon_\mathrm{p,n} = \langle\boldsymbol{u}\cdot(\boldsymbol{u}\cdot\nabla)\boldsymbol{u}\rangle_\mathrm{s} + \langle\boldsymbol{u}\cdot(\boldsymbol{u}\cdot\nabla)b\rangle_\mathrm{s} \tag{7c}$$

$$= \langle\nabla\cdot(\boldsymbol{u}E_\mathrm{k})\rangle_\mathrm{s} + \left\langle\nabla\cdot\left(\boldsymbol{u}E_\mathrm{p}\right)\right\rangle_\mathrm{s}, \tag{7d}$$

$$\varepsilon_\mathrm{t} = -\langle\partial_t E_\mathrm{t}\rangle_\mathrm{s} = \varepsilon_\mathrm{m} + \varepsilon_\mathrm{s} + \varepsilon_\mathrm{n} + \varepsilon_\mathrm{a}, \tag{7e}$$

where $\langle\ldots\rangle_\mathrm{s}$ indicates a spatial average over the whole domain, ε_t is the total change of flow energy over time, ε_m is the resolved part of the molecular dissipation, ε_s is the dissipation of an explicit SGS parametrisation scheme, ε_n is the numerical dissipation due to the discretisation of the advection term in a periodic domain without fixed walls, and ε_a is the additional numerical dissipation due to the Coriolis, buoyancy and pressure terms as well as the temporal discretisation. Note that the equality $\boldsymbol{u}\cdot(\boldsymbol{u}\cdot\nabla)\boldsymbol{u} = \nabla\cdot(\boldsymbol{u}E_\mathrm{k})$ used in the derivation of the energy transport equations is valid for exact continuous operators, but is only an approximation in case of discrete numerical operators.

3. Numerical methods

a. The INCA model

With our flow solver INCA, the Boussinesq equations are discretised by a fractional step method on a staggered Cartesian mesh. The code offers different discretisation schemes depending on the application, two of which are described below. For time advancement the explicit third-order Runge–Kutta scheme of Shu (1988) is used. The time-step is dynamically adapted to satisfy a Courant–Friedrichs–Lewy condition.

The spatial discretisation is a finite-volume method. We use a 2nd order central difference scheme for the discretisation of the diffusive terms and for the pressure Poisson solver. The Poisson equation for the pressure is solved at every Runge–Kutta sub step. The Poisson solver employs the fast Fourier-transform in the vertical (i.e. ζ) direction and a Stabilised Bi-Conjugate Gradient (BiCGSTAB) solver (van der Vorst 1992) in the horizontal ($x_{\parallel}$-$y_{\perp}$) plane.

b. The Adaptive Local Deconvolution Method

The Adaptive Local Deconvolution Method (ALDM) is based on the idea of using the discretisation error as an SGS parametrisation for turbulence (implicit LES, ILES). Given the one-dimensional generic transport equation for the quantity u

$$\partial_t u + \partial_x F(u) = 0, \tag{8}$$

the numerical approximation of the flux $\tilde{F}$ is computed based on the available filtered numerical solution $\overline{u}$ by approximately reconstructing the unfiltered solution $\tilde{u}$ and applying a numerical regularisation.

The reconstruction of the unfiltered solution on the represented scales is based on Harten-type deconvolution polynomials. Different polynomials are dynamically weighted depending on the

smoothness of the filtered solution. The regularisation is obtained through a tailored numerical flux function operating on the reconstructed solution. Both the solution-adaptive polynomial weighting and the numerical flux function involve free model parameters that were calibrated in such a way that the truncation error of the discretised equations optimally represents the SGS stresses of isotropic turbulence (Hickel et al. 2006). This set of parameters was not changed for any subsequent applications of ALDM. For the presented computations, we used an implementation of ALDM with improved computational efficiency (Hickel and Adams 2007).

The extension of ALDM to passive scalar transport was developed by Hickel et al. (2007). Remmler and Hickel (2012) showed that the method also performs well for the active scalar in stably stratified turbulent flows governed by the Boussinesq equations. They simplified the numerical flux function using the filtered divergence-free velocity field as the transporting velocity. The buoyancy flux in the x_j direction for an equidistant staggered grid then reads

$$\tilde{F}^s_{j\pm1/2} = \overline{v}_{j-1/2\pm1/2} \frac{\tilde{b}^-_{j\pm1/2} + \tilde{b}^+_{j\pm1/2}}{2} - \sigma_{j\pm1/2} \left[\tilde{b}^+_{j\pm1/2} - \tilde{b}^-_{j\pm1/2} \right], \tag{9}$$

where the numerical diffusivity is chosen to be

$$\sigma_{j\pm1/2} = \sigma_b \left| \tilde{v}^-_{j\pm1/2} - \tilde{v}^+_{j-1\pm1/2} \right| \tag{10}$$

with $\sigma_b = 0.615$ (Hickel et al. 2007). In these equations the index $j \pm 1/2$ indicates the right/left cell face (the velocity $\overline{v}_j$ is stored on the cell faces and the buoyancy $\overline{b}_j$ is stored in the cell centers), $\tilde{b}^+$ and $\tilde{b}^-$ are reconstructed solution values primarily based on values of $\overline{b}$ on the right/left of the reconstruction position.

The formulation (10) was chosen in analogy to ALDM for the momentum equations and is consistent with turbulence theory. It proved to work very well in fully turbulent flows. In the present case, however, the flow is temporarily laminar, which means that $\left| \tilde{v}^-_{j\pm1/2} - \tilde{v}^+_{j-1\pm1/2} \right|$ approaches

zero and the SGS regularisation is effectively turned off. Any numerical oscillations in a passive scalar field can then grow without bound. In order to regularise the scalar transport in case of advection by a smooth velocity field, we propose a blending of ALDM with an upwind biased flux function. A pure upwind flux function can be obtained within the given framework through

$$\sigma_{j\pm1/2}\big|_{\text{upwind}} = \frac{1}{2}\left|\overline{v}_{j-1/2\pm1/2}\right|. \tag{11}$$

The convex combination of standard ALDM flux and upwind flux leads to the following expression for the numerical viscosity:

$$\begin{aligned}\sigma_{j\pm1/2} = \alpha\sigma_b \underbrace{\left|\tilde{v}^-_{j\pm1/2} - \tilde{v}^+_{j-1\pm1/2}\right|}_{\mathscr{M}} \\ + \ (1-\alpha)\sigma_b \underbrace{\left|\frac{\tilde{v}^-_{j\pm1/2} + \tilde{v}^+_{j-1\pm1/2}}{2}\right|}_{\mathscr{P}},\end{aligned} \tag{12}$$

where we took the liberty of approximating the advection velocity by

$$\overline{v}_{j-1/2\pm1/2} \approx \frac{\tilde{v}^-_{j\pm1/2} + \tilde{v}^+_{j-1\pm1/2}}{2}. \tag{13}$$

The blending parameter α is dynamically evaluated based on the instantaneous velocity values by

$$\alpha = \frac{\mathscr{M}}{\beta\mathscr{P} + \mathscr{M}}, \tag{14}$$

where $\mathscr{M}$ denotes the velocity difference and $\mathscr{P}$ the advection velocity as defined in equation (12) and β is a free parameter. The choice of β controls the ratio $\mathscr{M}/\mathscr{P}$ at which the modification will become effective. In turbulent flows where velocity fluctuations are typically large compared to the mean advection velocity we find $\mathscr{M}/\mathscr{P} \gg \beta$, which means that $\alpha \to 1$ and we recover the original formulation (10). On the other hand, if the flow is laminar or governed by a large mean advection velocity, then $\alpha \to 0$ and we have an upwinding scheme.

c. Dynamic Smagorinsky Method

The Smagorinsky (1963) scheme is based on the assumption that the incompressible momentum SGS term can be parametrised as

$$\mathscr{F} = -\nabla \cdot \boldsymbol{\tau}^{mod} = -2\nabla \cdot \left(\nu_{\mathrm{t}} \overline{\boldsymbol{S}}\right) \tag{15}$$

where $\overline{S}_{ij} = 0.5\left(\partial_{x_i}\overline{v}_j + \partial_{x_j}\overline{v}_i\right)$ is the filtered strain rate tensor and $\boldsymbol{\tau}^{mod}$ is the parametrised SGS stress tensor. The unknown eddy viscosity ν_{t} is evaluated from the strain rate tensor via

$$\nu_{\mathrm{t}} = \left(C_{\mathrm{S}}\overline{\Delta}\right)^2 \left|\overline{S}\right| \; ; \quad \left|\overline{S}\right| = \sqrt{2\overline{S}_{ij}\overline{S}_{ij}} \, , \tag{16}$$

where $\overline{\Delta} = \left(\Delta_x \Delta_y \Delta_z\right)^{1/3}$ is either the grid size or the filter size. In this formulation, the unknown SGS fluxes can be computed directly from the resolved velocity field. The same closure can be used for scalar transport equations using an eddy diffusivity $\mu_{\mathrm{t}} = \nu_{\mathrm{t}}/\mathrm{Pr}_{\mathrm{t}}$.

The value of the model constant C_{S} is unknown a priori but can be estimated by means of the dynamic procedure of Germano et al. (1991). Given a solution available in its filtered form $\overline{v}$ with a grid filter width $\overline{\Delta}$. This filtered velocity field is explicitly filtered by a test filter with a larger filter width $\widehat{\Delta}$. As a test filter, we use a top-hat filter with $\widehat{\Delta} = 2\overline{\Delta}$. The subfilter-scale stress tensor is $T_{ij} = \widehat{\overline{u_i u_j}} - \widehat{\overline{u}_i}\widehat{\overline{u}_j}$. It cannot be computed directly from the filtered velocity field, but one can compute the Leonard stress tensor $L_{ij} = \widehat{\overline{u_i}\overline{u_j}} - \widehat{\overline{u}_i}\widehat{\overline{u}_j}$. Using the Germano identity

$$T_{ij} = L_{ij} + \widehat{\tau_{ij}} \tag{17}$$

and the standard Smagorinsky method for τ_{ij} and T_{ji}, we can minimise the difference between L_{ij} and

$$\begin{aligned} L_{ij}^{mod} &= T_{ij}^{mod}(C, \widehat{\Delta}, \widehat{\overline{\boldsymbol{v}}}) - \widehat{\tau_{ij}^{mod}}(C, \overline{\Delta}, \overline{\boldsymbol{v}}) \\ &= -2C\widehat{\Delta}^2 |\widehat{\overline{S}}| \widehat{\overline{S}}_{ij} + 2C\left(\widehat{\overline{\Delta}^2 |\overline{S}| \overline{S}_{ij}}\right) \\ &= 2CM_{ij}, \end{aligned} \tag{18}$$

where $C \equiv C_S^2$, by a least-squares procedure, yielding the optimal value (Lilly 1992)

$$C = \frac{1}{2} \frac{\left\langle L_{ij} M_{ij} \right\rangle_{\mathrm{s}}}{\left\langle M_{ij} M_{ij} \right\rangle_{\mathrm{s}}} \,. \tag{19}$$

A spatial average can be applied to both the numerator and denominator of (19) in order to prevent numerical instability. In the 3-D cases we apply this spatial average in the $y_\perp$-direction, while in the 2.5-D simulations we do not apply any average. We update the model parameter C at the beginning of every time step. For the turbulent Prandtl number we use a constant value of $\mathrm{Pr_t} = 0.4$ (see, e.g. Eidson 1985). We also performed numerical experiments using $\mathrm{Pr_t} = 0.2$ and $\mathrm{Pr_t} = 0.6$ (not shown) and found that the exact value of $\mathrm{Pr_t}$ is of minor importance to the overall simulation results.

d. Central discretisation scheme

In order to evaluate the benefit of an SGS parametrisation, we run underresolved direct numerical simulations with an ordinary 4th order accurate central interpolation, namely

$$\tilde{u}^{-}_{j+1/2} = \frac{1}{12} \left(-\overline{u}_{j-2} + 7\,\overline{u}_{j-1} + 7\,\overline{u}_{j} - \overline{u}_{j-2} \right) \tag{20}$$

on an LES grid, i.e. at a resolution much too low to resolve the Kolmogorov scale.

4. Test cases

According to Prusa et al. (1996) gravity waves arriving at the upper mesosphere tend to be almost monochromatic with horizontal wavelengths ranging from a few kilometres to more than 100 km and with vertical wavelengths of a few kilometres. These waves break at altitudes between 65 km and 120 km. We investigate three different cases of monochromatic gravity waves in an environment representative of the upper mesosphere at an altitude of approximately 80 km. For the atmospheric parameters see tab. 1 and for the wave parameters see tab. 2. All three waves

have a wavelength of 3 km and the wave phase is such that, in the rotated coordinate system, the maximum total buoyancy gradient within the wave is located at $\zeta = 750\,\mathrm{m}$ and the minimum (associated with the least stable point) at $\zeta = 2250\,\mathrm{m}$. The primary and secondary perturbations of the waves used to construct the initial condition for the 3-D simulations were computed by Fruman et al. (2014). In fig. 2 we show the initial perturbation energy E_{ini} (primary and secondary perturbations) as a function of ζ, integrated in the spanwise–streamwise ($x_{\parallel}$-$y_{\perp}$) plane.

Case 1 is a statically unstable inertia-gravity wave with a wave period of 8 hours and a phase speed of $0.1\,\mathrm{m\,s^{-1}}$. The wavelength of the leading transverse normal mode (primary perturbation) is somewhat longer than the base wavelength ($\lambda_{\parallel} = 3.98\,\mathrm{km}$), while the leading secondary singular vector (with respect to an optimisation time of 5 minutes) has a significantly shorter wavelength ($\lambda_{\perp} = 0.4\,\mathrm{km}$). The initial perturbation energy (fig. 2(a)) is distributed rather homogeneously in the wave with a peak close to the minimum static stability and a minimum in the most stable region. The time scales of the turbulent wave breaking and of the wave propagation are similarly long, which makes this case especially interesting. Remmler et al. (2013) pointed out that a secondary breaking event is stimulated in this cases when the most unstable part of the wave reaches the region where the primary breaking has earlier generated significant turbulence.

Case 2 is also an inertia-gravity wave with the same period and phase speed as case 1, but with an amplitude below the threshold of static instability. The wave is perturbed by the leading transverse primary singular vector ($\lambda_{\parallel} = 2.115\,\mathrm{km}$), and the leading secondary singular vector ($\lambda_{\perp} = 300\,\mathrm{m}$). An optimisation time of 7.5 minutes was used for computing both the primary and secondary singular vectors. The perturbation energy in this case is concentrated exclusively in the region of lowest static stability (see fig. 2(b)). This is typical for SV, which maximise perturbation energy growth in a given time. Despite the wave being statically stable, the perturbations lead to a weak breaking and the generation of turbulence. However, the duration of the breaking event is much

shorter than the wave period and the overall energy loss in the wave is not much larger than the energy loss through viscous forces on the base wave in the same time.

Case 3 is a statically unstable high-frequency gravity wave with a period of 15 minutes and a phase speed of $3.3\,\mathrm{m\,s^{-1}}$ perturbed with the leading transverse primary normal mode ($\lambda_{\parallel} = 2.929\,\mathrm{km}$) and the leading secondary singular vector with $\lambda_{\perp} = 3\,\mathrm{km}$. The initial perturbation energy (fig. 2(c)) has a clear maximum at $\zeta = 100\,\mathrm{m}$, which is in a region with moderately stable stratification. The breaking is much stronger than in cases 1 and 2 and lasts for slightly more than one wave period. Turbulence and energy dissipation are almost uniformly distributed in the domain during the most intense phase of the breaking.

The three different cases were chosen to represent a wide range of different configurations of breaking gravity waves. They especially differ in the duration of the breaking compared to the wave period. In case 1 the breaking duration is slightly smaller than the wave period and the breaking involves multiple bursts of turbulence. In case 2 the breaking lasts only for a short time compared to the wave period and in case 3 the breaking lasts longer than one wave period.

5. Case 1: unstable inertia-gravity wave

a. Three-dimensional DNS

Fruman et al. (2014) showed that in 2.5-D simulations a small initial random disturbance of the flow field can lead to different global results. In order to investigate whether the same applies to full 3-D simulations of the same case and whether the LES method has an influence on this variability, we added two new DNS simulations ($640 \times 64 \times 500$ cells) to the results of Remmler et al. (2013) to have a very small ensemble of four simulations from which we can compute averages and standard deviations. For these new simulations, a very small amount of white noise

was added to all three velocity components at the initial time. In fig. 3 we show the ensemble average of the amplitudes $\langle a \rangle_{\mathrm{e}}$ and of the spatially averaged total dissipation rate $\langle \varepsilon_{\mathrm{t}} \rangle_{\mathrm{s,e}}$ as a solid line and the standard deviation from these ensemble averages as shaded area.

For the present case the wave breaking consists of a series of three single breaking events. Each of those events is characterised by a peak in the energy dissipation and by an enhanced amplitude decrease. The strongest breaking event is initialised by the initial perturbations and starts directly at the beginning of the simulation. It involves overturning and generation of turbulence in the whole computational domain. The intensity of this primary breaking event is very similar in all ensemble members, independent of the resolution and initial white noise. The second breaking event around $t \approx 4\,\mathrm{h}$ is preceeded by an instability of the large-scale wave and generates only a small amount of turbulence in the unstable half of the domain. The third breaking event around $t \approx 5\,\mathrm{h}$ is caused by a small amount of remaining turbulence from the first breaking event, which was generated in the stable part of the wave. At the time of the third breaking event the wave phase has travelled approximately half a wavelength and so the unstable part of the wave has reached the region of the remaining turbulence at this time. For details of the wave breaking process, we refer to Remmler et al. (2013) and Fruman et al. (2014).

The amplitude variations in the 3-D DNS are very small. The ensemble members diverge slightly during a very weak breaking event at $t \approx 8\,\mathrm{h}$, which has very different intensity in the four simulations. The total dissipation rate varies significantly among the ensemble members during the weak breaking events but not during the first strong breaking event.

b. Three-dimensional LES

We simulated the 3-D setup of case 1 using three different LES resolutions, which we refer to as fine ($100 \times 24 \times 80$ cells, corresponding to a cell size of $39.8\,\mathrm{m} \times 17.7\,\mathrm{m} \times 37.5\,\mathrm{m}$), medium

(24 × 12 × 80 cells) and coarse (24 × 12 × 20 cells). We chose these resolutions after a series of numerical experiments which showed two main results: (i) the horizontal (i.e. in the $x_{\parallel}$-$y_{\perp}$ plane) resolution can be reduced without much effect on the global result as long as the vertical resolution remains comparatively high, and (ii) reducing the vertical resolution and keeping the horizontal resolution high had a strong adverse effect on the global result, independent of the LES method used. One reason for this behaviour might be the insufficient resolution of the initial perturbation on the coarsest grid. From fig. 2(a) it is obvious that the initial perturbation is well resolved by 80 cells in the ζ direction, but deviates in places on the coarse grid with only 20 cells in the ζ direction.

In LES it is easily affordable to run small ensembles for many different simulations. For all presented 3-D LES results we performed the same simulation eight times with some low-level white noise superposed on the initial condition (consisting of the base wave and its leading primary and secondary perturbations) and once with no added noise. The results of these nine realisations were then averaged. The average amplitudes of simulations with three different resolutions and four different LES methods (standard ALDM with $\beta = 0.0$, modified ALDM with $\beta = 0.01$, Dynamic Smagorinsky [DSM], and plain central discretisation [CDS4]) are shown in figs. 3(a) to 3(c). Figure 3(d) shows the total dissipation rates for the medium grid. In all figures the error bars indicate the standard deviation of the ensemble.

Using the fine LES grid the average wave amplitude is quite well predicted by standard ALDM, DSM and CDS4. Modified ALDM dissipates slightly too much energy while standard ALDM shows very large variations between ensemble members.

With the medium grid the three SGS models (i.e. DSM and the two versions of ALDM) yield good agreement with the DNS, both in the average amplitude and in the variations among ensemble members. Only CDS4 (without SGS model) creates a bit too much dissipation and far too much

variability. The analysis of the total dissipation rates in fig. 3(d) shows that the exact evolution of the dissipation is reproduced by none of the LES methods. However, the results with modified ALDM, DSM and CDS4 are acceptably close to the DNS results. The result from standard ALDM strongly oscillates in time despite being an ensemble average. For clarity of the figure we did not plot the error bars for this curve, but it is nevertheless obvious that the variation among the ensemble members with standard ALDM is much larger than with the other methods.

With the coarse resolution ALDM and CDS4 dissipate far too much energy and hence predict a too-quick wave decay. The flow physics are not correctly reproduced. Only DSM produces an acceptable result, although the wave amplitude at the end of the breaking is considerably lower than in the DNS. The variability in the DSM results is even smaller than in the DNS, which is not necessarily an indication of a good approximation of the unresolved turbulent scales.

The strong variations of the wave amplitude (fine resolution) and total dissipation rate (medium resolution) in the simulations with standard ALDM motivated the development of the modification described in section 3b. In fig. 4 we compare Hovmöller diagrams of resolved kinetic energy dissipation (as an indicator of velocity fluctuations) averaged in $x_{\parallel}$-$y_{\perp}$ planes from the DNS and the high resolution LES with DSM, and with standard and modified ALDM. Standard ALDM produces a lot of velocity oscillations in the stable half of the domain ($0\,\mathrm{m} < \zeta < 1500\,\mathrm{m}$) not present in the DNS and DSM results. These velocity fluctuations are generated by numerical oscillations in the buoyancy which are due to the smooth velocity field that causes the numerical diffusivity to be effectively zero. These oscillations are thus only slightly smoothed but not completely eliminated by the stable stratification. If we add a passive scalar to the flow with a similar initial distribution as the buoyancy, we observe indeed exponentially growing fluctuations up to the limits of double precision floating point numbers. These physically unlikely oscillations can be avoided by modifying the flux function for the scalar as described in section 3b. The parameter

β controls the intensity of the damping. In a series of numerical experiments we found $\beta = 0.01$ to be a good compromise between excessive damping with strong wave decay (higher values of β) and no damping with strong oscillations (lower values of β). Choosing the exact value of β is, at the present time, a matter of personal judgement.

The first breaking event lasts for about one hour and is associated with the strongest turbulence. This peak is predicted quite differently by the different SGS models. We show the energy dissipation during the first two hours in fig. 5. In the ALDM and DSM simulations only a minor part of the total energy dissipation is resolved due to the coarse resolution, the remainder is provided by the implicit (ε_n) or explicit (ε_s) turbulence SGS parametrisation. This is exactly how the parametrisation is supposed to work. However, the total dissipation during the most intense breaking is considerably smaller than in the DNS with both SGS parametrisations.

For the CDS4 simulations, where no SGS parametrisation is applied (fig. 5(e)) the resolved dissipation ε_m is much higher due to the stronger small-scale fluctuations (see also the spectra in fig. 6 described below). During the phase of highest dissipation it is complemented by a small amount of numerical dissipation ε_n and a significant amount of dissipation ε_a due to numerical effects in terms other than the advective term. The resulting total dissipation ε_t matches surprisingly well with the DNS result.

The energy dissipation can be decomposed into mechanical energy dissipation ε_k and thermal energy dissipation ε_p. In figs. 5(b), 5(d) and 5(f) we show $\varepsilon_\mathrm{p} = \varepsilon_\mathrm{p,m} + \varepsilon_\mathrm{p,n} + \varepsilon_\mathrm{p,s}$ and the total energy dissipation. In the simulations with ALDM the thermal energy dissipation ε_p is too strong compared to the total energy dissipation ε_t during the peak. With DSM ε_p is smaller, but the ratio $\varepsilon_\mathrm{p}/\varepsilon_\mathrm{t}$ is also smaller than in the DNS. In CDS4, on the other hand, ε_p is too small during the period of peak dissipation. After the first dissipation peak, after about one hour, the dissipation rates match the DNS results quite well with all three LES methods. In all LES the dissipation

peaks a little bit earlier than in the DNS. The time difference is surely due to the time that flow energy needs to be transported through the spectrum from the finest LES scales to the scales of maximum dissipation in the DNS.

Instantaneous vertical energy spectra averaged in the $x_{\parallel}$ and $y_{\perp}$ directions are shown in fig. 6. The chosen instant in time in each case is at the moment of maximum dissipation (which is a slightly different time in each simulation) and at $t = 2\,\mathrm{h}$, which is after the first breaking event. At the time of maximum dissipation the agreement between all of the LES and the DNS in terms of E_{t} and E_{k} is quite good. With the DSM the small-scale fluctuations are a bit underpredicted and with CDS4 they are overpredicted. With ALDM (standard and modified) the matching is good also at the smallest resolved scales. The difference between standard ALDM and the modified version is small due to the fully developed turbulence at this time. The potential energy spectrum with ALDM and DSM has the right level, but does not decrease monotonically as in the DNS. The E_{p}-spectrum with CDS4 is much closer to the DNS result than in the other LES solutions with only the high-wavenumber fluctuations a bit overpredicted.

At $t = 2\,\mathrm{h}$ the agreement of the E_{k}-spectra from all LES methods with the DNS is even better than at the time of maximum dissipation. The spectral slope is a bit too steep with DSM, a bit too shallow with CDS4 and somewhere in between with ALDM, with the modified version of ALDM slightly outperforming the original ALDM. The E_{p}-spectrum is well predicted by all four LES methods in the wavelength range $\lambda_{\zeta} \gtrsim 500\,\mathrm{m}$. At smaller scales the DNS spectrum suddenly falls off, which is not reproduced with any of the LES methods. The level of turbulence is already quite low at this time, so there is a clear difference in the spectra between the original and modified ALDM, the result with the modified ALDM agreeing better with the DNS than the original version.

c. 2.5-D simulations

The results of the 2.5-D simulations (DNS and LES) are summarised in fig. 7. Corresponding to the 3-D LES, we chose LES grids with high (100×80 cells), medium (24×80 cells) and coarse (24×20 cells) resolution and performed the same LES eight times with some low-level white noise superposed on the initial condition (consisting of the base wave and its leading primary perturbation) and once with no added noise. The results of these nine realisations were then averaged. The reference 2.5-D DNS were run at a resolution of 660×500 cells (see Fruman et al. 2014). An ensemble of eight DNS was used for the calculation of mean values and standard deviations. For a detailed comparison of 2.5-D and 3-D DNS results see Fruman et al. (2014).

The results obtained with the highest LES resolution are very close to the DNS reference results (figs. 7(a,b)), almost independent of the LES method used. The best results, both in terms of wave amplitude a and total energy dissipation ε_t were obtained with ALDM in the standard formulation. Since the spurious oscillations observed in some 3-D LES simulations with ALDM did not occur in any of the 2.5-D simulations, we do not present any results using the modified ALDM with $\beta > 0$. With DSM the final wave amplitude is a bit too low, while the total dissipation rate matches quite well with the DNS result throughout the whole simulated period. With pure CDS4, on the other hand, the final wave amplitude is a little bit too high. The total dissipation rate has some deviations from the 2.5-D DNS in some regions. Specifically, there is a peak (in mean value and variability) after approximately 5.5 hours, which is not present in the 2.5-D DNS but which did occur in the 3-D DNS.

With a grid coarsened in the $x_{\|}$ direction (figs. 7(c,d)), the CDS4 method becomes less reliable. The amplitude decay is strongly overpredicted and the variability among ensemble members is much larger than in the DNS. With ALDM and DSM the results are very similar: during the

first hour the dissipation is a bit too high, but this is compensated for later on and the final wave amplitude is predicted quite well.

The grid further coarsened in the ζ direction causes the CDS4 simulations to quickly break down. The ALDM and DSM simulations are stable, but the quality of the result is poor, showing too much total energy dissipation and wave amplitude decay.

d. Summary of case 1

The unstable IGW is the most complex test case presented here. It involves multiple breaking events and the total time of the breaking is similar to the wave period. It is thus a challenging test for the LES methods in 3-D and 2.5-D. In 3-D LES we obtained good agreement with the reference DNS using the DSM and ALDM (with $\beta = 0.01$). With the original ALDM ($\beta = 0.0$) there are spurious oscillations in the stable half of the domain that reduce the overall result quality. The LES using the CDS4 method, although utilising neither explicit nor implicit numerical viscosity, remain stable throughout all simulations. A certain pile-up of energy close to the grid cut-off wavenumber is visible in the spectra, but due to the low overall turbulence level it is not strong enough to cause the simulations to diverge.

The 3-D and 2.5-D LES results depend strongly on the numerical resolution in the ζ direction (of the wave phase), while the resolution in the $x_{||}$ direction has only minor influence on the results. With a resolution of 80 cells in the ζ direction the results are generally in good agreement with the DNS, while basically all simulations with a ζ-resolution of only 20 cells deviate strongly from the reference DNS.

6. Case 2: Stable inertia-gravity wave

a. Three-dimensional DNS

The reference DNS results are taken from Fruman et al. (2014). They presented simulations with $720 \times 96 \times 1024$ cells and with $512 \times 64 \times 768$ cells. To have at least a small ensemble of four members for comparison, we repeated these simulations (adding low level white noise to the velocity components of the initial condition) running until $t = 1\,\mathrm{h}$. The ensemble average and standard deviation of these four simulations is shown in fig. 8.

The breaking of the wave is weaker than in the unstable IGW case and it lasts only for a short period in time. The initial perturbations grow during the first minutes and generate some turbulence, which remains confined to the least stable part of the domain and is dissipated quickly. The dissipation peak occurs at $t = 11\,\mathrm{min}$ and 30 min later the turbulence has vanished completely.

b. Three-dimensional LES

The computational domain for the stable inertia-gravity wave is smaller in the $x_{\parallel}$ and $y_{\perp}$ directions than for the unstable wave in case 1. In order to have approximately the same cell size for the LES as for case 1 we chose an LES grid with $64 \times 12 \times 80$ cells (corresponding to a cell size of $33.0\,\mathrm{m} \times 25.0\,\mathrm{m} \times 37.5\,\mathrm{m}$) for the highest LES resolution. After experimenting with different coarsening levels in the $x_{\parallel}$ and ζ directions we found the most interesting results with one grid coarsened in the $x_{\parallel}$ direction with $16 \times 12 \times 80$ cells and another coarsened in the ζ direction with $64 \times 12 \times 20$ cells. With a fully coarsened grid of $16 \times 12 \times 20$ cells, the model performance was as poor as for case 1. The initial perturbation energy (fig. 2(b) is well resolved by the fine LES grid and the grid coarsened in the $x_{\parallel}$ direction, but probably insufficiently resolved on the grid coarsened in the ζ direction.

We performed LES using ALDM ($\beta = 0$, $\beta = 10^{-2}$, $\beta = 10^{-5}$), DSM and CDS4. With the fine LES grid, the DSM and CDS4 results agree well with the DNS in terms of base wave amplitude (fig. 8(a)) and total dissipation rate (fig. 8(b)). The original ALDM introduces spurious oscillations in the buoyancy and consequently also in the velocity field, as in case 1. These oscillations manifest themselves in strong fluctuations of the total dissipation rate, and the wave amplitude decays a little bit too strongly. The modified ALDM with additional damping ($\beta = 10^{-2}$) avoids these spurious oscillations at the cost of a too high energy dissipation rate after the breaking event when the flow has become almost laminar. The results do not strongly depend on the exact value of β. For $\beta = 10^{-5}$ we obtain a very similar result as for $\beta = 10^{-2}$, only the dissipation rate of the laminar wave is slightly smaller. If the value of β is further decreased, a similar solution as with the unmodified ALDM is obtained. We could not find a value that yields low dissipation and supresses oscillations at the same time.

With the grid coarsened in the $x_{\|}$ direction (figs. 8(c) and 8(d)), the DSM and CDS4 results do not differ very much from those with the fine grid. In both cases the single dissipation peak has become multiple peaks, but the total dissipation during the breaking event remains approximately the same. With the original ALDM the spurious oscillations are weaker than with the fine grid but still apparent. As with the fine grid, ALDM with additional damping eliminates these oscillations. With $\beta = 10^{-2}$ the dissipation rate is again slightly too high, resulting in a too-rapid amplitude decay, but with $\beta = 10^{-5}$ the result agrees very well with the DNS and with the LES using DSM and CDS4.

If the grid is not coarsened in the $x_{\|}$ direction but in the direction of the base wave ζ (figs. 8(e) and 8(f)), all LES methods fail to predict the wave amplitude and dissipation rate correctly. This is consistent with the findings for case 1 (unstable IGW). Especially with ALDM the dissipation rates are far too high. With DSM and CDS4 the shape of the dissipation peak is not predicted correctly

and the partial recovery of the base wave amplitude in the last phase of the breaking is too weak, so the predicted final wave amplitude after the breaking is too low, although the dissipation rate in the re-laminarised wave is overpredicted only slightly.

c. 2.5-D simulations

The results of the 2.5-D simulations (DNS and LES) are summarised in fig. 9. As for the 3-D LES, we chose LES grids with high resolution (64×80 cells)and grids coarsened in the $x_{\|}$ direction (16×80 cells) and in the ζ direction (64×20 cells), and we performed the same LES eight times with some low-level white noise superposed on the initial condition (consisting of the base wave and its leading primary perturbation) and once with no added noise. The results of these nine realisations were then averaged. The reference 2.5-D DNS were run at a resolution of 350×55. An ensemble of six DNS was used for the calculation of mean values and standard deviations. For a detailed comparison of 2.5-D and 3-D DNS results see Fruman et al. (2014).

The matching of the simulation results is very similar to the 3-D cases. With the highest resolution (64×80 cells), the agreement is almost perfect, independent of the LES method used. With the grid coarsened in the $x_{\|}$ direction (16×80 cells) there are some small deviations from the DNS, but the overall agreement is still good, except that with ALDM the dissipation and amplitude decay at the end of the simulation are a bit too high. With the grid coarsened in the ζ direction (64×20 cells), the results are equally wrong with all three LES methods. The dissipation and amplitude decay are strongly overpredicted during the whole simulation.

d. Summary of case 2

The breaking of the stable IGW is weak and lasts only for a fraction of the wave period. Both in 3-D and in 2.5-D LES we obtained good agreement with the reference DNS as long as we chose

a comparatively high resolution in the ζ direction, while the results were not much affected by choosing a low resolution in the $x_{\|}$ direction. Since the 2.5-D DNS were sufficient for estimating the breaking duration and intensity, see Fruman et al. (2014), LES with only $16 \times 80 = 1280$ cells are thus sufficient for computing the basic characteristic of the wave breaking. Good LES results were obtained without any SGS parametrisation and with DSM.

7. Case 3: Unstable high-frequency gravity wave

a. Three-dimensional DNS

Fruman et al. (2014) simulated the case of a breaking unstable HGW on grids with 1536^3 cells, 768^3 cells and 384^3 cells. They found no notable differences between the two highest resolutions. We added another two simulations with 768^3 cells and 384^3 cells and averaged the results of these five DNS. The results are presented in fig. 10.

The wave breaking is much more intense than in both IGW cases. The generation of turbulence starts immediately after the initialisation in the unstable part of the wave and is quickly advected also into the stable part due to the high phase velocity of the wave. At the time of maximum energy dissipation (around $t = 15\,\mathrm{min}$) turbulence is distributed almost homogeneously in the whole domain. The non-dimensional wave amplitude rapidly decreases from an initial value of $a = 1.2$ to $a \approx 0.3$ after 30 min and does not change significantly any more after that time. The breaking process is analysed in more detail by Fruman et al. (2014).

b. Three-dimensional LES

The domain for the unstable high-frequency gravity wave case is almost cubic. In a number of LES with different resolutions in the horizontal and the vertical directions we could not find any indication that different resolutions in the different directions make a great deal of difference.

Hence we present here the results of three LES grids with coarse (20^3), medium (40^3) and fine (80^3), the fine resolution corresponding to a cell size of $36.6\,\mathrm{m} \times 37.5\,\mathrm{m} \times 37.5\,\mathrm{m}$) resolution. On the medium and fine grid, the initial perturbation is resolved almost perfectly (see fig. 2(c)), while on the coarse grid there are some slight deviations in the initial perturbation energy distribution. We performed LES on these grids using ALDM ($\beta = 0$, $\beta = 0.01$), DSM and CDS4. For all of these cases we averaged the results of nine simulations to get an estimate of the ensemble average and the standard deviations.

With the high LES resolution of 80^3 cells, the results are very similar to the DNS (figs. 10(a) and 10(b)). The base wave amplitude decay is slightly overpredicted with ALDM and CDS4, but the amplitude remains almost within the variations among the DNS ensemble members. The peak dissipation rate matches well with the DNS in all cases. With CDS4 the dissipation falls off a bit too rapidly after the peak. With modified ALDM ($\beta = 0.01$) the dissipation rate is overpredicted during the phases of weak turbulence, i.e. before and after the peak. Actually, using the modified version is not necessary for this simulation, since no physically unlikely oscillations develop at any time due to the high level of turbulence during most of the simulation.

When the resolution is reduced to 40^3 cells (figs. 10(c) and 10(d)) the main difference is in the CDS4 simulations. The turbulence during the peak of breaking is too strong and the molecular dissipation is not sufficient on the coarse grid to keep the energy balance. Energy piles up at the smallest resolved wavenumbers (see the energy spectra in fig. 12) and numerical errors lead to an increase of flow total energy, which eventually also affects the largest resolved scales, and therefore the amplitude of the base wave. The time of simulation break-down is almost the same in all ensemble members. By using the turbulence parametrisation schemes this instability can be avoided. The best matching with the DNS results is obtained with the original ALDM. Only about 10% of the peak energy dissipation is resolved, see fig. 11(a), but the sum of resolved molecular

and numerical dissipation matches quite well with the DNS result. Also the ratio between ε_k and ε_p is well repoduced, see fig. 11(b). The modified ALDM dissipates too much energy. The DSM predicts a slightly too-high base wave amplitude after the breaking and the total dissipation rate starts oscillating moderately after approximately 60 min. The total dissipation rate presented in fig. 11(c) is overpredicted a bit at the peak, but matches well with the DNS before $t = 10$ min and after $t = 15$ min.

In fig. 12 we present the energy spectra of all LES with 40^3 cells compared to the DNS spectra. The CDS4 spectra are wrong, as mentioned above, and the method fails for this case. The ALDM and DSM spectra are very close to the DNS reference for wavelengths $\lambda_\zeta > 400$ m. For smaller wavelengths the spectral energy is slightly underpredicted with only very small differences between ALDM ($\beta = 0.0$) and DSM. With ALDM ($\beta = 0.01$), the thermal energy dissipation ε_p is overpredicted, hence the spectra of potential and total energy fall off to rapidly close to the grid cut-off wavelength.

The results obtained with the coarsest grid, with 20^3 cells (figs. 10(e) and 10(f)), are similar to those with the medium resolution. The simulations with CDS4 break down due to unbounded growth of numerical errors. ALDM with $\beta = 0.01$ is far too dissipative before and after the peak of dissipation. The DSM now underpredicts the final wave amplitude and generates oscillations of total dissipation after the breaking. The closest match with the DNS is obtained with the original ALDM, both in terms of base wave amplitude and total dissipation rate. Also the variations among ensemble members are similar to the DNS. The onset of dissipation is, in all LES a little bit earlier than in the DNS. This is consistent with our observations in case 1.

c. 2.5-D simulations

The results of the 2.5-D simulations (DNS and LES) are summarised in figure 13. LES grids with high (80^2 cells), medium (40^2 cells) and coarse resolution (20^2 cells) were used. The same LES were performed eight times with some low-level white noise superposed on the initial condition (consisting of the base wave and its leading primary perturbation) and once with no added noise. The results of these nine realisations were then averaged. The reference 2.5-D DNS were run at a resolution of 500×500 cells. An ensemble of six DNS was used for the calculation of mean values and standard deviations.

With the highest resolution (80^2 cells), the results in terms of wave amplitude and total dissipation rate are in very close agreement with the reference DNS. Only for CDS4 is the dissipation rate a bit too low during the period of decreasing dissipation.

At the medium resolution (40^2 cells), the DSM and ALDM results are very similar and still in good agreement with the DNS. The dissipation peak is slightly shifted to earlier times according to the dissipation acting at larger wavenumbers and the hence reduced time required for flow energy to reach this range. CDS4, however, predicts the wrong evolution of the wave amplitude and dissipation rate and cannot be recommended for this resolution.

At the coarsest resolution (20^2 cells), ALDM and DSM still do a very good job in predicting the amplitude decay and the dissipation maximum. The dissipation peak is further shifted forward in time due to the reduced time the flow energy needs to move through the spectrum. In the CDS4 simulation, however, the dissipation rate becomes negative after approximately 20 minutes and hence the predicted flow field is completely wrong, although the simulations remain stable in a numerical sense during the whole simulated period.

d. Summary of case 3

The unstable HGW involves much stronger turbulence than the IGW cases and thus the buoyancy forces are weaker compared to the acceleration associated with turbulent motions. The original ALDM and the DSM thus do an excellent job in predicting the dissipation rates and the wave amplitude decay over time, even at a very coarse resolution with a cell size of about $\Delta = 150\,\mathrm{m}$, both in 3-D and 2.5-D simulations. According to Fruman et al. (2014) the 3-D and the 2.5-D solutions are similar in this case. We conclude that for a proper estimation of the key parameters breaking time, maximum dissipation and amplitude decay only a 2.5-D simulation with $20^2 = 400$ cells is necessary, if ALDM or DSM is applied.

8. Conclusion

We scrutinised different methods of large-eddy simulation for three cases of breaking monochromatic gravity waves. The methods tested included: the Adaptive Local Deconvolution Method (ALDM), an implicit turbulence parametrisation; the dynamic Smagorinsky method (DSM); and a plain fourth order central discretisation without any turbulence parametrisation (CDS4). The test cases have been carefully designed and set-up by Remmler et al. (2013) and Fruman et al. (2014) based on the primary and secondary instability modes of the base waves and included an unstable and a stable inertia-gravity wave as well as an unstable high-frequency gravity wave. All simulations presented were run in 2.5-D and 3-D domains and for all simulations a small ensemble of simulations starting from slightly different initial conditions were performed in order to assess the sensitivity and robustness of the results.

The original ALDM leads to spurious oscillations of the buoyancy field in some 3-D simulations, where the velocity field is very smooth for a long time. We thus developed a modified version of

the ALDM flux function. The modification led to a significant reduction of the oscillations, but also increased the overall energy dissipation.

For all three test cases we started at an LES resolution of 80 cells per wavelength of the original wave and gradually reduced the resolution in all three directions. The inertia-gravity wave cases, in which the wave vector almost coincides with the vertical direction, were very sensitive to the resolution in the direction of the wave vector, while the resolution in the other directions could be strongly reduced without a massive negative effect on the overall results.

We found that results obtained with ALDM and DSM are generally in good agreement with the reference direct numerical simulations as long as the resolution in the direction of the wave vector is sufficiently high. The CDS4 simulations, without turbulence parametrisation, are only successful if the resolution is high and the level of turbulence comparatively low. In cases with low turbulence intensity and a smooth velocity field for long time periods (unstable and stable IGW) ALDM generated spurious oscillations in the buoyancy field, which we could avoid by using the modified numerical flux function. However, this was not necessary in the case with a high turbulence level (unstable HGW) and in all 2.5-D simulations.

Our results back the findings of Remmler and Hickel (2012, 2013, 2014), who showed that both DSM and ALDM are suitable tools for the simulation of homogeneous stratified turbulence. Applying the same methods to gravity-wave breaking, where turbulence is spatially inhomogeneous and intermittent in time, reveals that DSM is in some cases more robust than ALDM, although ALDM provides a better approximation of the spectral eddy viscosity and diffusivity in homogeneous stratified turbulence (Remmler and Hickel 2014).

In all simulations we observed that the peak of dissipation occurs earlier in simulations with coarser computational grids. This is more pronounced in 2.5-D LES, but also apparent in 3-D LES. We explain this time difference by the time required for flow energy to move from the

smallest resolved wavenumbers in an LES to the dissipative scales in a DNS. Among the tested LES methods there is no method that can account for this time lag. However, the large-scale flow and the maximum dissipation can still be predicted correctly.

Fruman et al. (2014) have shown that in some cases 2.5-D simulations can be sufficient to get a good estimate of the energy dissipation during a breaking event. We showed that with ALDM and DSM reliable results can be obtained in 2.5-D simulations with less than 2000 computational cells. Such inexpensive simulations will allow running large numbers of simulations in order to study the influence of various parameters on wave breaking, such as stratification, wavelength, amplitude, propagation angle and viscosity. A possible automated approach would involve computing the growth rates of perturbations of the original waves, setting up an ensemble of 2.5-D LES initialised by the base wave and its leading primary perturbation and extracting key data from the LES results, such as the maximum energy dissipation, the amplitude decay and the duration of the breaking event. Another potential application of our findings is the (2.5-D or 3-D) simulation of wave packets in the atmosphere, which is computationally feasible only if small-scale turbulence remains unresolved and is treated by a reliable subgrid-scale parametrisation such as ALDM or DSM.

Acknowledgment. U. A. and S. H. thank Deutsche Forschungsgemeinschaft for partial support through the MetStröm (Multiple Scales in Fluid Mechanics and Meteorology) Priority Research Program (SPP 1276), and through Grants HI 1273/1-2 and AC 71/4-2. Computational resources were provided by the HLRS Stuttgart under the grant DINSGRAW.

References

Achatz, U., 2005: On the role of optimal perturbations in the instability of monochromatic gravity waves. *Phys. Fluids*, **17 (9)**, 094107.

712 Achatz, U. and G. Schmitz, 2006a: Optimal growth in inertia-gravity wave packets: Energetics,
713 long-term development, and three-dimensional structure. *J. Atmos. Sci.*, **63**, 414–434.

714 Achatz, U. and G. Schmitz, 2006b: Shear and static instability of inertia-gravity wave packets:
715 Short-term modal and nonmodal growth. *J. Atmos. Sci.*, **63**, 397–413.

716 Afanasyev, Y. D. and W. R. Peltier, 2001: Numerical simulations of internal gravity wave breaking
717 in the middle atmosphere: The influence of dispersion and three-dimensionalization. *J. Atmos.*
718 *Sci.*, **58**, 132–153.

719 Andreassen, Ø., P. Øyvind Hvidsten, D. C. Fritts, and S. Arendt, 1998: Vorticity dynamics in a
720 breaking internal gravity wave. Part 1. Initial instability evolution. *J. Fluid Mech.*, **367**, 27–46.

721 Baldwin, M. P., et al., 2001: The quasi-biennial oscillation. *Rev. Geophys.*, **39**, 179–229.

722 Chun, H.-Y., M.-D. Song, J.-W. Kim, and J.-J. Baik, 2001: Effects of gravity wave drag induced
723 by cumulus convection on the atmospheric general circulation. *J. Atmos. Sci.*, **58 (3)**, 302–319.

724 Dörnbrack, A., 1998: Turbulent mixing by breaking gravity waves. *J. Fluid Mech.*, **375**, 113–141.

725 Dunkerton, T. J., 1997: Shear instability of internal inertia-gravity waves. *J. Atmos. Sci.*, **54**, 1628–
726 1641.

727 Eidson, T. M., 1985: Numerical simulation of the turbulent Rayleigh–Bénard problem using sub-
728 grid modelling. *J. Fluid Mech.*, **158**, 245–268.

729 Fritts, D. C. and M. J. Alexander, 2003: Gravity wave dynamics and effects in the middle atmo-
730 sphere. *Rev. Geophys.*, **41 (1)**.

731 Fritts, D. C. and L. Wang, 2013: Gravity wave-fine structure interactions. Part II: Energy dissipa-
732 tion evolutions, statistics, and implications. *J. Atmos. Sci.*, **70 (12)**, 3710–3734.

733 Fritts, D. C., L. Wang, J. Werne, T. Lund, and K. Wan, 2009: Gravity wave instability dynamics at
734 high reynolds numbers. Parts I and II. *J. Atmos. Sci.*, **66 (5)**, 1126–1171.

735 Fritts, D. C., L. Wang, and J. A. Werne, 2013: Gravity wave-fine structure interactions. Part I:
736 Influences of fine structure form and orientation on flow evolution and instability. *J. Atmos. Sci.*,
737 **70 (12)**, 3710–3734.

738 Fruman, M. D. and U. Achatz, 2012: Secondary instabilities in breaking inertia-gravity waves. *J.*
739 *Atmos. Sci.*, **69**, 303–322.

740 Fruman, M. D., S. Remmler, U. Achatz, and S. Hickel, 2014: On the construction of a direct
741 numerical simulation of a breaking inertia-gravity wave in the upper-mesosphere. *J. Geophys.*
742 *Res.*, **119**, 11 613–11 640.

743 Germano, M., U. Piomelli, P. Moin, and W. H. Cabot, 1991: A dynamic subgrid-scale eddy vis-
744 cosity model. *Phys. Fluids A*, **3 (7)**, 1760–1765.

745 Grimsdell, A. W., M. J. Alexander, P. T. May, and L. Hoffmann, 2010: Model study of waves
746 generated by convection with direct validation via satellite. *J. Atmos. Sci.*, **67 (5)**, 1617–1631.

747 Hickel, S. and N. A. Adams, 2007: A proposed simplification of the adaptive local deconvolution
748 method. *ESAIM*, **16**, 66–76.

749 Hickel, S., N. A. Adams, and J. A. Domaradzki, 2006: An adaptive local deconvolution method
750 for implicit LES. *J. Comput. Phys.*, **213**, 413–436.

751 Hickel, S., N. A. Adams, and N. N. Mansour, 2007: Implicit subgrid-scale modeling for large-eddy
752 simulation of passive scalar mixing. *Phys. Fluids*, **19**, 095 102.

753 Hickel, S., C. Egerer, and J. Larsson, 2014: Subgrid-scale modeling for implicit large eddy sim-
754 ulation of compressible flows and shock-turbulence interaction. *Phys. Fluids*, **26**, 106 101, doi:
755 10.1063/1.4898641.

756 Hickel, S., T. Kempe, and N. A. Adams, 2008: Implicit large-eddy simulation applied to turbulent
757 channel flow with periodic constrictions. *Theor. Comput. Fluid Dyn.*, **22**, 227–242.

758 Hines, C. O., 1965: Dynamical heating of the upper atmosphere. *J. Geophys. Res.*, **70 (1)**, 177–
759 183.

760 Hines, C. O., 1997: Doppler-spread parameterization of gravity-wave momentum deposition in
761 the middle atmosphere. Part 1: Basic formulation. *J. Atmos. Sol.-Terr. Phys.*, **59 (4)**, 371–386.

762 Kim, Y.-J., S. D. Eckermann, and H.-Y. Chun, 2003: An overview of the past, present and future
763 of gravity–wave drag parametrization for numerical climate and weather prediction models.
764 *Atmosphere-Ocean*, **41 (1)**, 65–98.

765 Lelong, M.-P. and T. J. Dunkerton, 1998: Inertia-gravity wave breaking in three dimensions. Parts
766 I and II. *J. Atmos. Sci.*, **55**, 2473–2501.

767 Lilly, D. K., 1992: A proposed modification of the german subgrid-scale closure method. *Phys.*
768 *Fluids A*, **4 (3)**, 633–635.

769 Lindzen, R. S., 1981: Turbulence and stress owing to gravity wave and tidal breakdown. *J. Geo-*
770 *phys. Res.*, **86**, 9707–9714.

771 Lund, T. S. and D. C. Fritts, 2012: Numerical simulation of gravity wave breaking in the lower
772 thermosphere. *J. Geophys. Res.*, **117 (D21105)**.

773 McFarlane, N. A., 1987: The effect of orographically excited gravity wave drag on the general
774 circulation of the lower stratosphere and troposphere. *J. Atmos. Sci.*, **44**, 1775–1800.

McLandress, C., 1998: On the importance of gravity waves in the middle atmosphere and their parameterization in general circulation models. *J. Atmos. Sol.-Terr. Phy.*, **60 (14)**, 1357–1383.

Muraschko, J., M. D. Fruman, U. Achatz, S. Hickel, and Y. Toledo, 2014: On the application of Wentzel–Kramer–Brillouin theory for the simulation of the weakly nonlinear dynamics of gravity waves. *Q. J. R. Meteorol. Soc.*, doi:10.1002/qj.2381.

O'Sullivan, D. and T. J. Dunkerton, 1995: Generation of inertia-gravity waves in a simulated life cycle of baroclinic instability. *J. Atmos. Sci.*, **52 (21)**, 3695–3716.

Plougonven, R. and C. Snyder, 2007: Inertia gravity waves spontaneously generated by jets and fronts. Part I: Different baroclinic life cycles. *J. Atmos. Sci.*, **64 (7)**, 2502–2520.

Prusa, J. M., P. K. Smolarkiewicz, and R. R. Garcia, 1996: Propagation and breaking at high altitudes of gravity waves excited by tropospheric forcing. *J. Atmos. Sci.*, **53 (15)**, 2186–2216.

Remmler, S., M. D. Fruman, and S. Hickel, 2013: Direct numerical simulation of a breaking inertia-gravity wave. *J. Fluid Mech.*, **722**, 424–436.

Remmler, S. and S. Hickel, 2012: Direct and large eddy simulation of stratified turbulence. *Int. J. Heat Fluid Flow*, **35**, 13–24.

Remmler, S. and S. Hickel, 2013: Spectral structure of stratified turbulence: Direct numerical simulations and predictions by large eddy simulation. *Theor. Comput. Fluid Dyn.*, **27**, 319–336.

Remmler, S. and S. Hickel, 2014: Spectral eddy viscosity of stratified turbulence. *J. Fluid Mech.*, **755 (R 6)**.

Rieper, F., S. Hickel, and U. Achatz, 2013: A conservative integration of the pseudo-incompressible equations with implicit turbulence parameterization. *Monthly Weather Review*, **141**, 861–886.

797 Shu, C.-W., 1988: Total-variation-diminishing time discretizations. *SIAM J. Sci. Stat. Comput.*,
798 **9 (6)**, 1073–1084.

799 Smagorinsky, J., 1963: General circulation experiments with the primitive equations. I: The basic
800 experiment. *Mon. Wea. Rev.*, **91**, 99–164.

801 Smith, R. B., 1979: The influence of mountains on the atmosphere. *Adv. Geophys.*, **21**, 87–230.

802 Vallis, G. K., 2006: *Atmospheric and oceanic fluid dynamics*. Cambridge University Press.

803 van der Vorst, H. A., 1992: Bi-CGSTAB: A fast and smoothly converging variant of Bi-CG for the
804 solution of nonsymmetric linear systems. *SIAM J. Sci. Stat. Comput.*, **13 (2)**, 631–644.

805 Winters, K. B. and E. A. D'Asaro, 1994: Three-dimensional wave instability near a critical level.
806 *J. Fluid Mech.*, **272**, 255–284.

LIST OF TABLES

TABLE 1. Atmosphere parameters.

Kinematic viscosity	ν	$1\,\mathrm{m}^2\mathrm{s}^{-1}$
Thermal diffusivity	μ	$1\,\mathrm{m}^2\mathrm{s}^{-1}$
Latitude for Coriolis parameter	ϕ_C	70N
Coriolis parameter	f	$1.37\times10^{-4}\,\mathrm{s}^{-1}$
Brunt-Väisälä frequency	N	$2\times10^{-2}\,\mathrm{s}^{-1}$
Gravitational acceleration	g	$9.81\,\mathrm{m\,s}^{-2}$

TABLE 2. Parameters of the initial conditions for the investigated test cases. A_1 and A_2 are the amplitudes of the respective perturbations in terms of the maximum perturbation energy density compared to the maximum energy density in the basic state; $\hat{u}_{\parallel}$, $\hat{v}_{\perp}$ and $\hat{b}$ are the amplitudes of the original wave (eq. 3); λ_y and λ_z are the horizontal and vertical wavelengths in the earth frame corresponding to the base wavelength $\lambda = 3\,\mathrm{km}$ and the propagation angle Θ; $\langle \varepsilon_t \rangle_{\max}$ is the maximum value observed in our respective highest resolved DNS.

Case	I. Unstable IGW	II. Stable IGW	III. Unstable HGW
Amplitude	$a = 1.2$	$a = 0.86$	$a = 1.2$
	$\hat{u}_{\parallel} = 8.97\,\mathrm{m\,s^{-1}}$	$\hat{u}_{\parallel} = 6.43\,\mathrm{m\,s^{-1}}$	$\hat{u}_{\parallel} = 0.23\,\mathrm{m\,s^{-1}}$
	$\hat{v}_{\perp} = 14.56\,\mathrm{m\,s^{-1}}$	$\hat{v}_{\perp} = 10.43\,\mathrm{m\,s^{-1}}$	$\hat{v}_{\perp} = 12.20\,\mathrm{m\,s^{-1}}$
	$\hat{b} = 0.229\,\mathrm{m\,s^{-2}}$	$\hat{b} = 0.164\,\mathrm{m\,s^{-2}}$	$\hat{b} = 0.244\,\mathrm{m\,s^{-2}}$
Propagation angle Θ	89.5°	89.5°	70°
Wavelengths	$\lambda_y = 343\,\mathrm{km}$	$\lambda_y = 343\,\mathrm{km}$	$\lambda_y = 8.7\,\mathrm{km}$
	$\lambda_z = 3.0\,\mathrm{km}$	$\lambda_z = 3.0\,\mathrm{km}$	$\lambda_z = 3.1\,\mathrm{km}$
Primary perturbation	NM, $\alpha = 90°$	SV, $\alpha = 90°$	NM, $\alpha = 90°$
	$\lambda_{\parallel} = 3.98\,\mathrm{km}$	$\lambda_{\parallel} = 2.12\,\mathrm{km}$	$\lambda_{\parallel} = 2.93\,\mathrm{km}$
	$A_1 = 0.05$	$A_1 = 0.05$	$A_1 = 0.05$
Secondary perturbation	$\lambda_{\perp} = 0.4\,\mathrm{km}$	$\lambda_{\perp} = 0.3\,\mathrm{km}$	$\lambda_{\perp} = 3.0\,\mathrm{km}$
	$A_2 = 0.02$	$A_2 = 0.01$	$A_2 = 0.01$
Wave period T	7.8 h (28 083 s)	7.8 h (28 083 s)	15.3 min (918 s)
Phase speed c_p	$0.107\,\mathrm{m\,s^{-1}}$	$0.107\,\mathrm{m\,s^{-1}}$	$3.27\,\mathrm{m\,s^{-1}}$
Maximum dissipation during breaking $\langle \varepsilon_t \rangle_{\max}$	$17\,\mathrm{mW\,kg^{-1}}$	$4.3\,\mathrm{mW\,kg^{-1}}$	$88\,\mathrm{mW\,kg^{-1}}$

LIST OF FIGURES

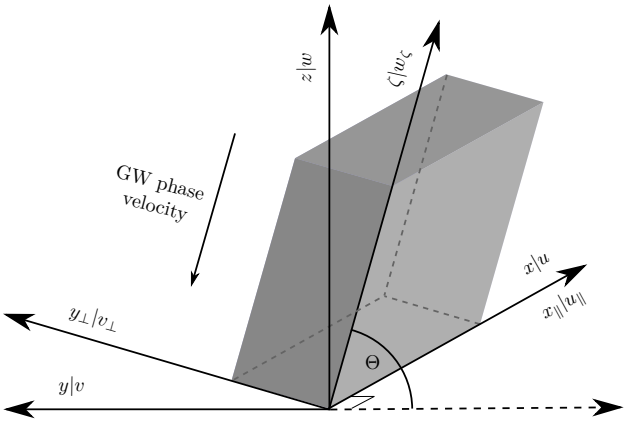

863 FIG. 1. Rotated coordinate system and computational domain (grey box) for the monochromatic gravity wave
864 (after Remmler et al. 2013).

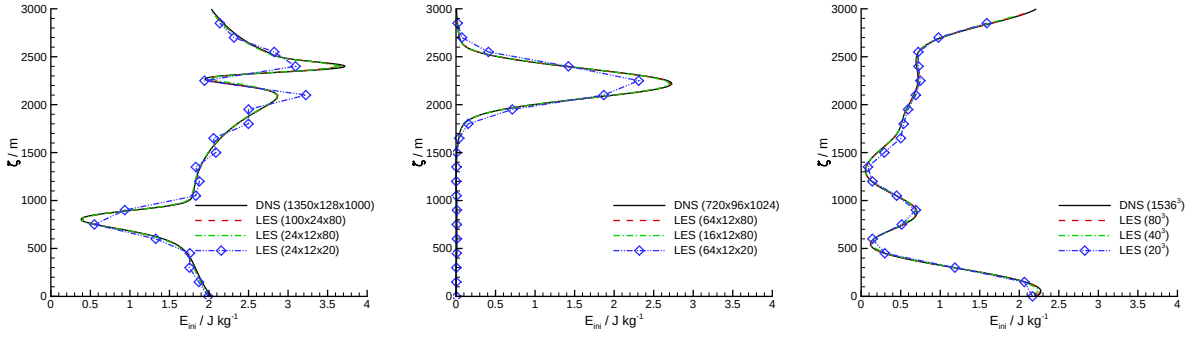

(a) unstable IGW (case 1) (b) stable IGW (case 2) (c) unstable HGW (case 3)

FIG. 2. Initial horizontally ($x_{\parallel}$-$y_{\perp}$) averaged perturbation energy at different 3-D grid resolutions.

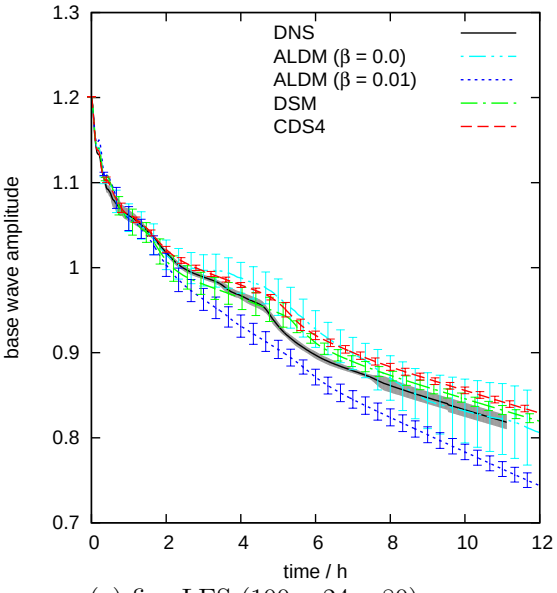

(a) fine LES ($100 \times 24 \times 80$): a

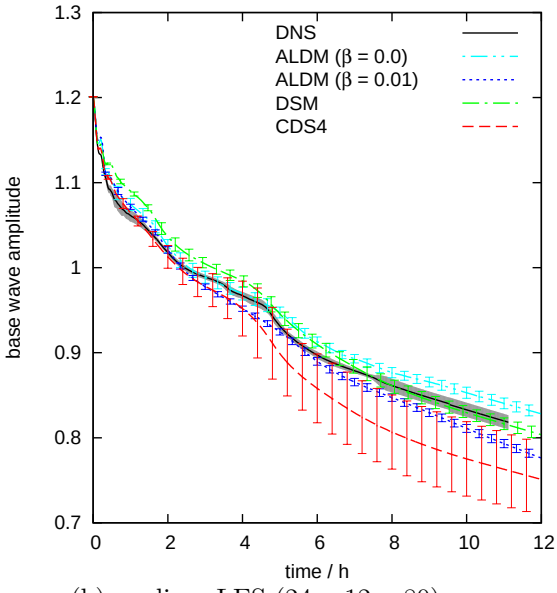

(b) medium LES ($24 \times 12 \times 80$): a

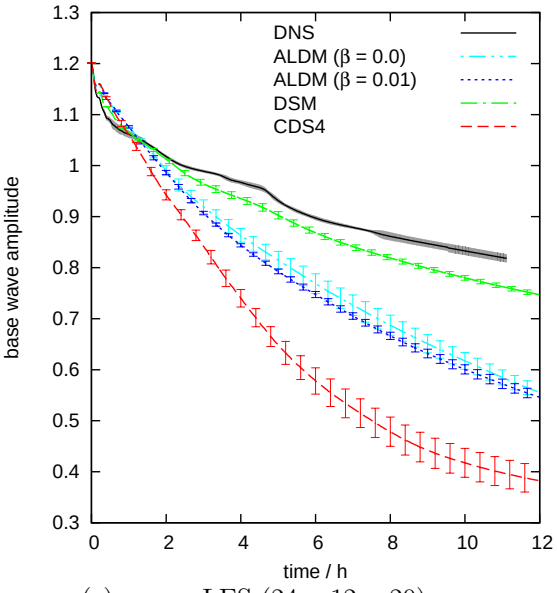

(c) coarse LES ($24 \times 12 \times 20$): a

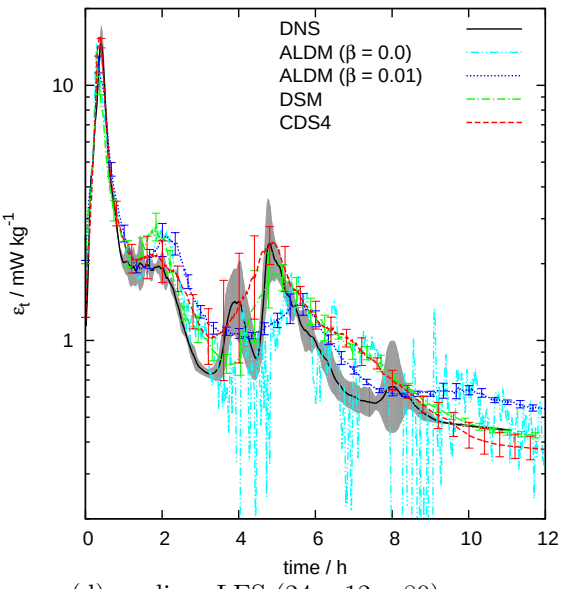

(d) medium LES ($24 \times 12 \times 80$): ε_t

FIG. 3. Statically unstable IGW (3-D): Base wave amplitudes a and total dissipation rates ε_t at coarse, medium and fine LES resolution. The grey shaded area indicates the standard deviation of four DNS and the error bars indicate the standard deviation of nine LES.

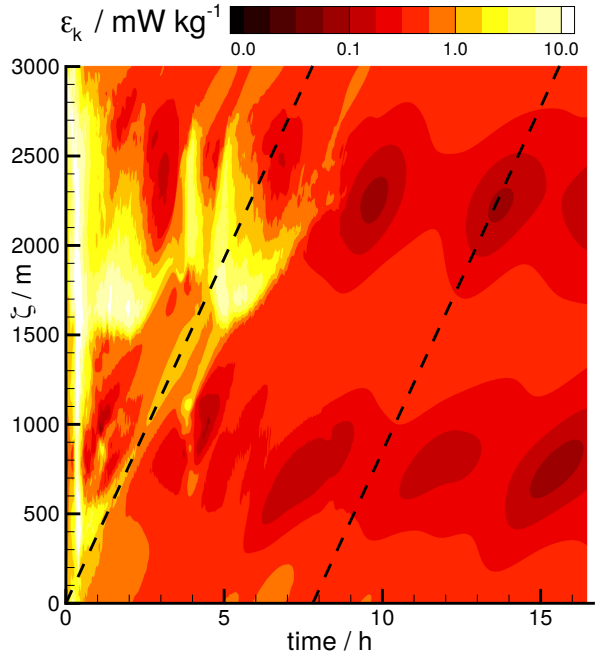

(a) DNS: ε_{k} / $\mathrm{mW\,kg^{-1}}$

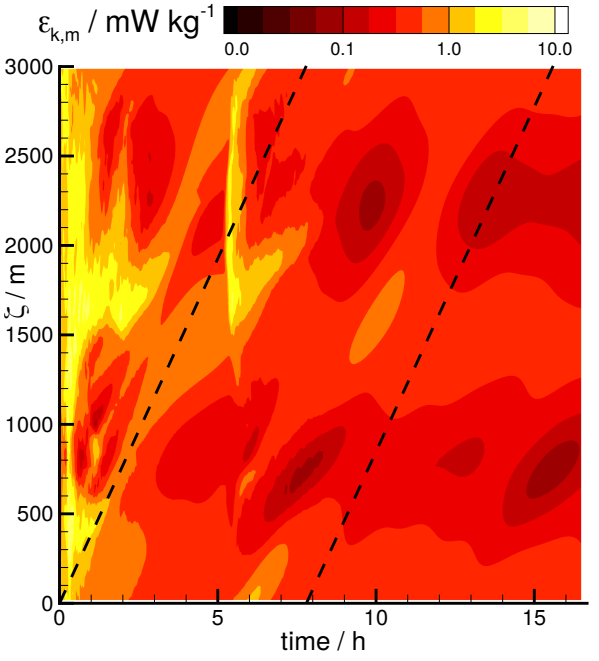

(b) DSM: $\varepsilon_{\mathrm{k,m}}$ / $\mathrm{mW\,kg^{-1}}$

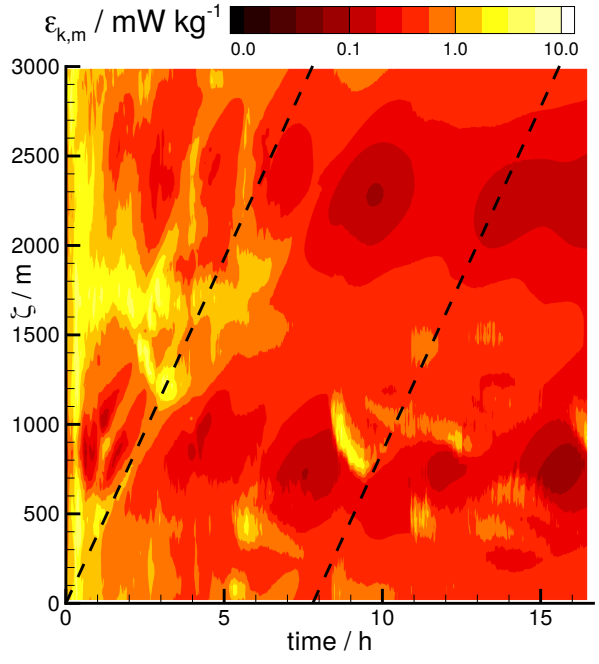

(c) ALDM ($\beta = 0.01$): $\varepsilon_{\mathrm{k,m}}$ / $\mathrm{mW\,kg^{-1}}$

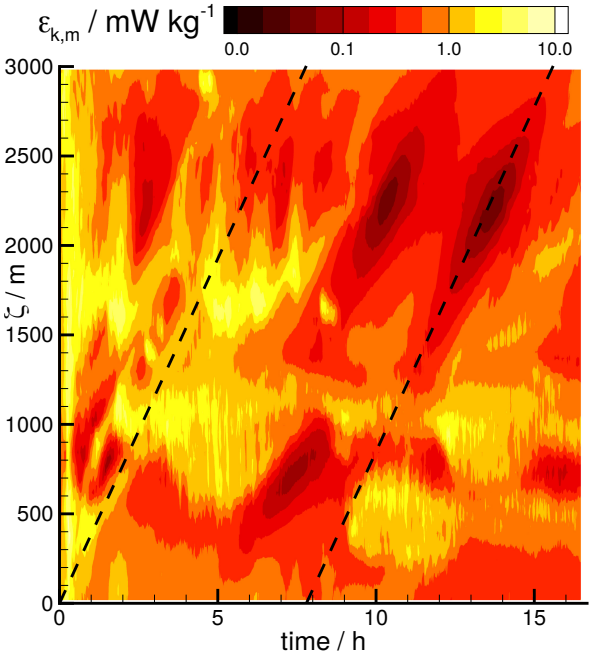

(d) ALDM ($\beta = 0$): $\varepsilon_{\mathrm{k,m}}$ / $\mathrm{mW\,kg^{-1}}$

FIG. 4. Statically unstable IGW (3-D): Hovmöller plots of horizontally averaged (resolved) dissipation of kinetic energy. Top left panel: DNS ($640 \times 64 \times 500$ cells), the other panels: LES ($100 \times 24 \times 80$ cells). The dashed line indicates a fixed position in space.

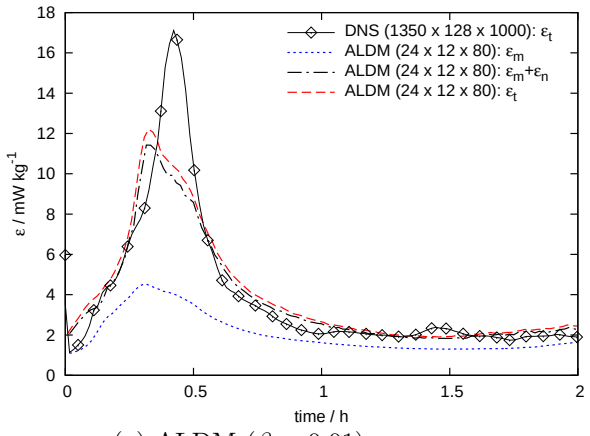

(a) ALDM ($\beta = 0.01$): ε_m, ε_n, ε_t

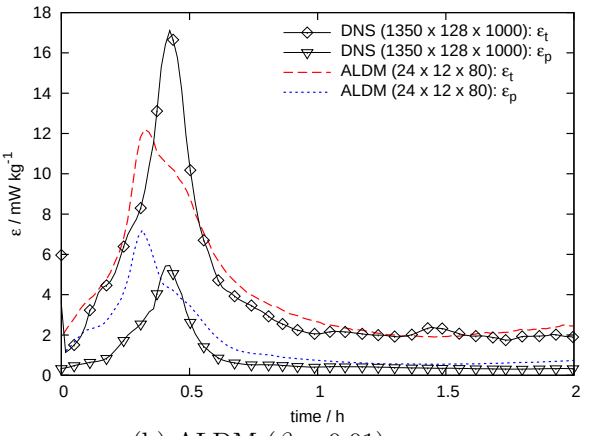

(b) ALDM ($\beta = 0.01$): ε_p, ε_t

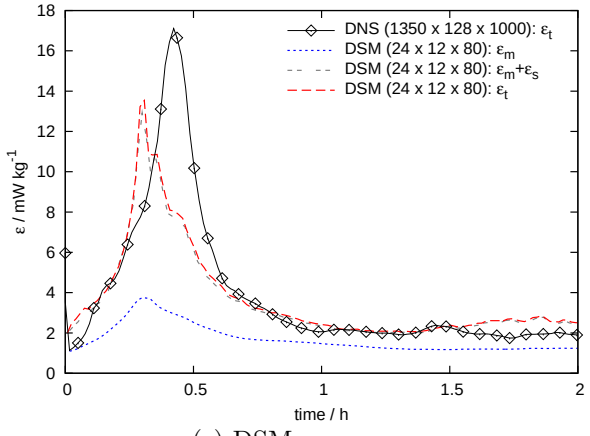

(c) DSM: ε_m, ε_s, ε_t

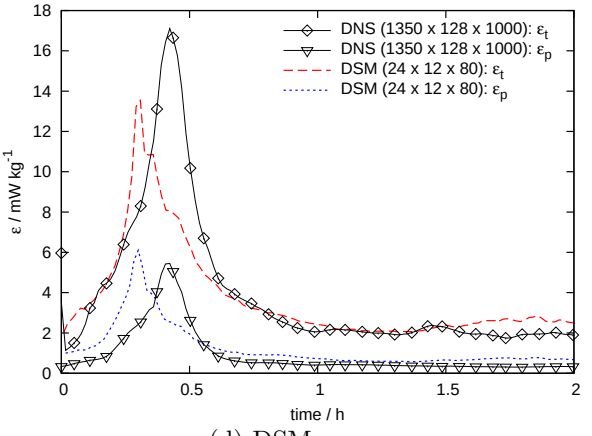

(d) DSM: ε_p, ε_t

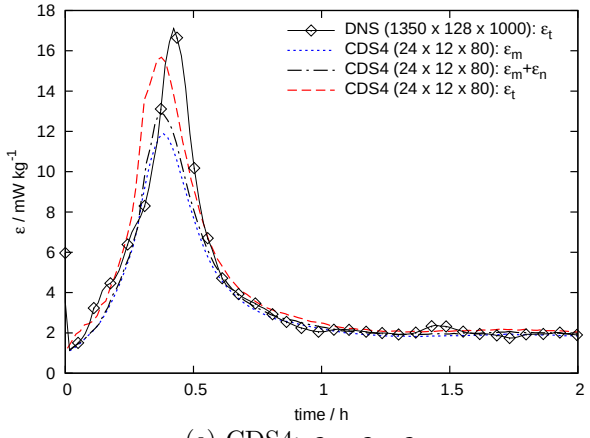

(e) CDS4: ε_m, ε_n, ε_t

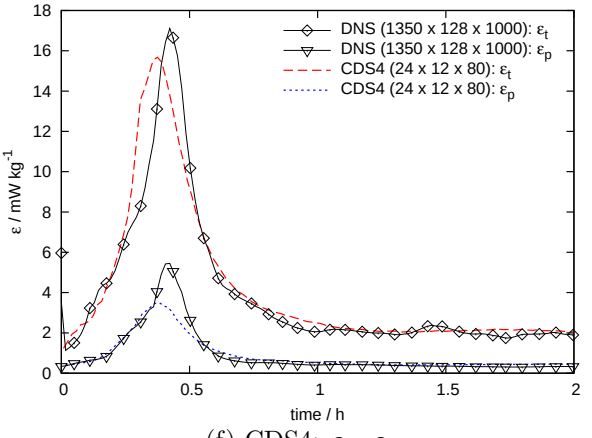

(f) CDS4: ε_p, ε_t

FIG. 5. Statically unstable IGW (3-D): Comparison of resolved (ε_m), numerical (ε_n), parametrised (ε_s) and total (ε_t) dissipation (left column) and thermal (ε_p) and total dissipation (right column) during the first breaking event (DNS: single simulation, LES: ensemble averages).

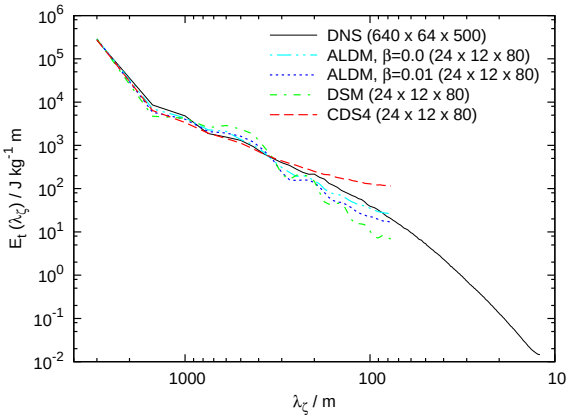

(a) E_t at max. dissipation

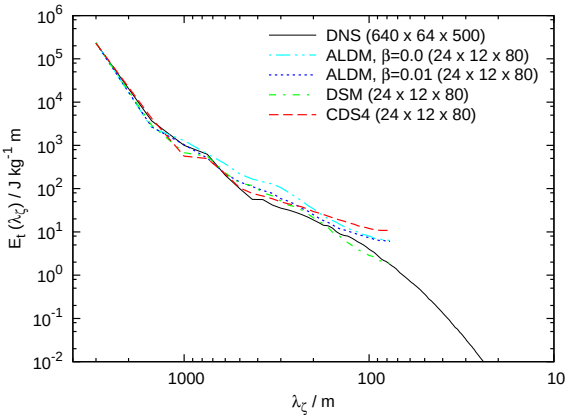

(b) E_t at $t = 2\,\mathrm{h}$

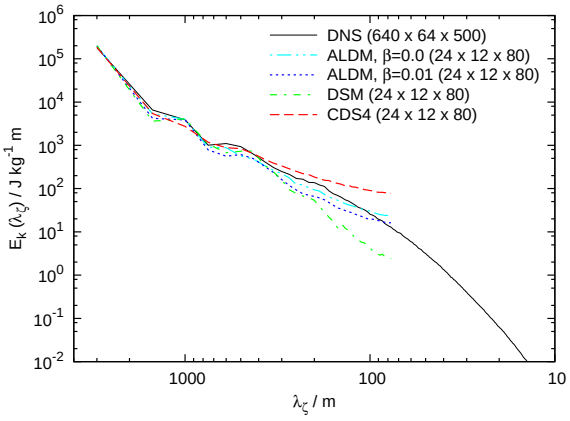

(c) E_k at max. dissipation

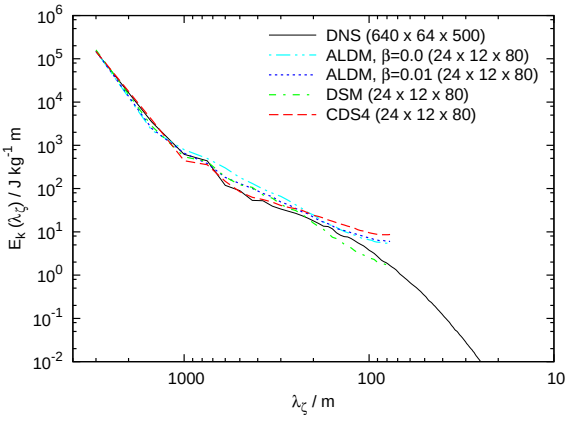

(d) E_k at $t = 2\,\mathrm{h}$

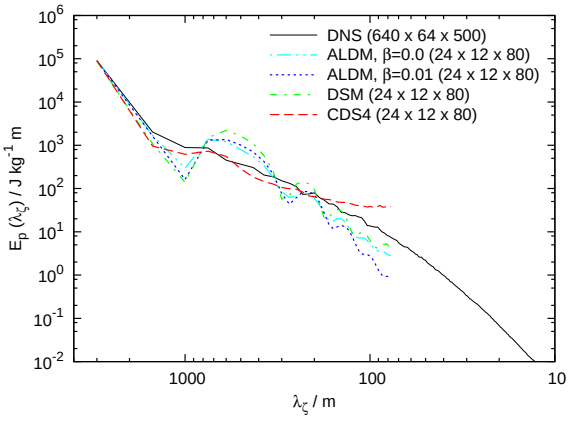

(e) E_p at max. dissipation

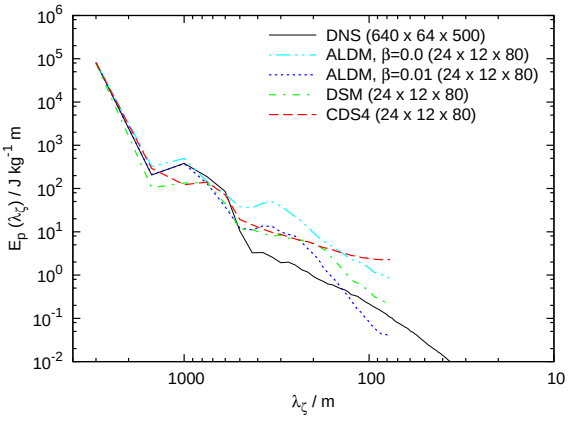

(f) E_p at $t = 2\,\mathrm{h}$

FIG. 6. Statically unstable IGW (3-D): Distributions of total, kinetic and potential energy over vertical wavelength λ_ζ at the moment of maximum total energy dissipation (left column) and at $t = 2$ hours (right column) (DNS: single simulation, LES: ensemble averages).

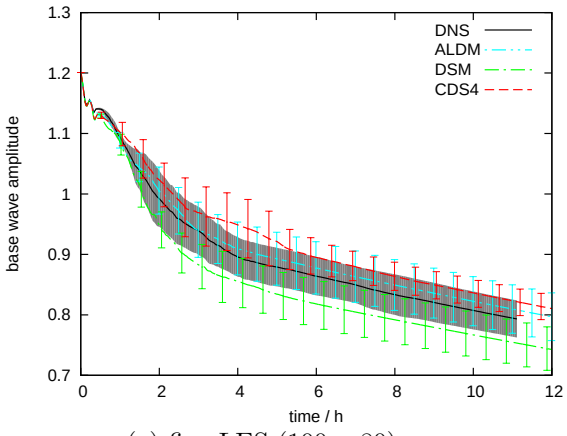

(a) fine LES (100×80): a

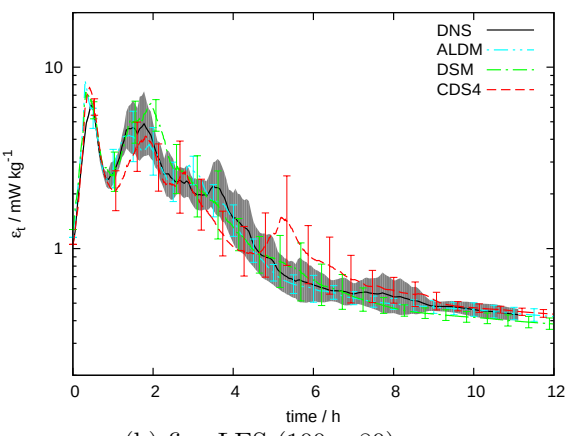

(b) fine LES (100×80): ε_t

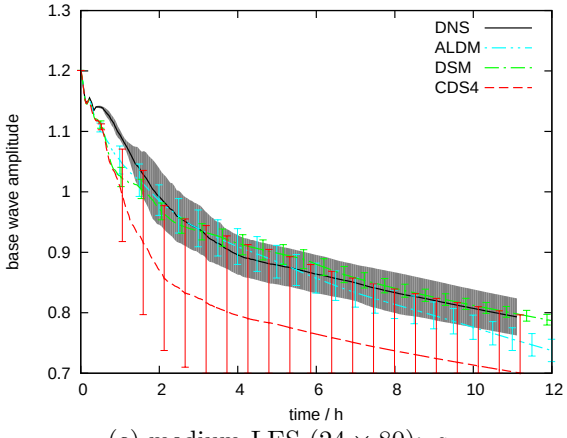

(c) medium LES (24×80): a

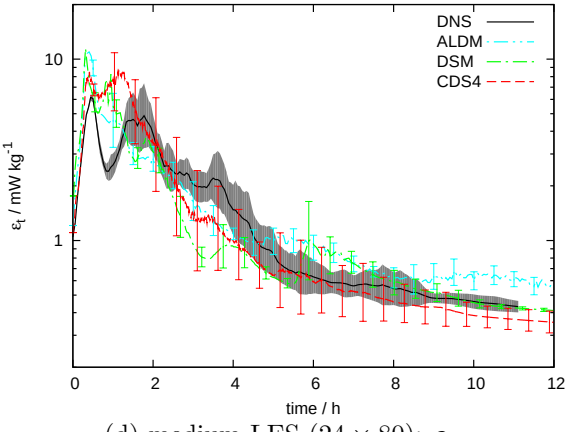

(d) medium LES (24×80): ε_t

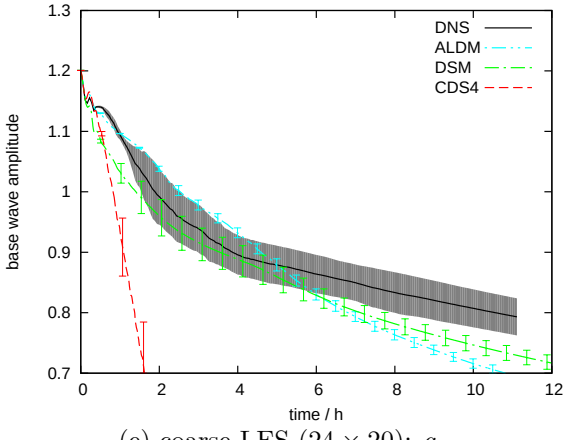

(e) coarse LES (24×20): a

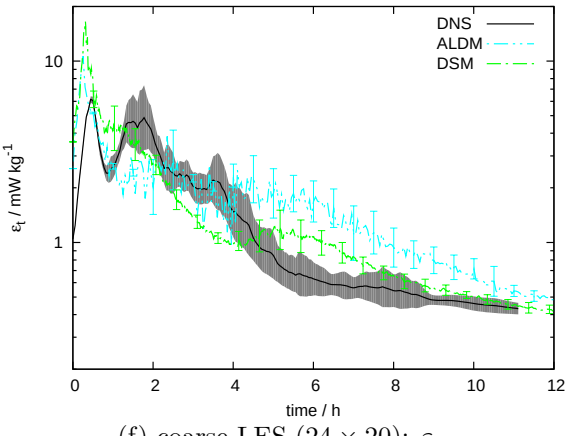

(f) coarse LES (24×20): ε_t

FIG. 7. Statically unstable IGW (2.5-D): Base wave amplitude a and total dissipation rate ε_t at coarse, medium and fine LES resolution compared with a and resolved dissipation rate ε_m from DNS. The grey shaded area indicates the standard deviation of eight DNS, the error bars indicate the standard deviation of nine LES.

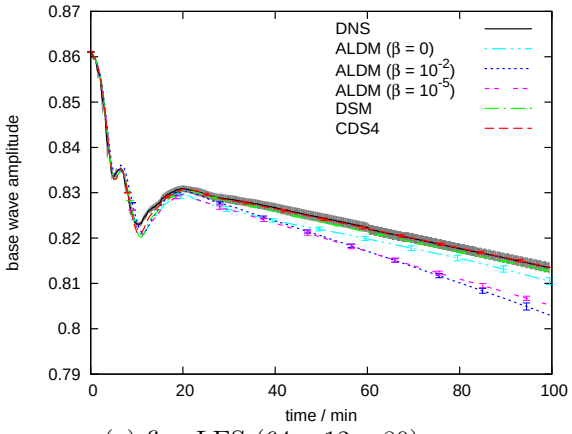

(a) fine LES ($64 \times 12 \times 80$): a

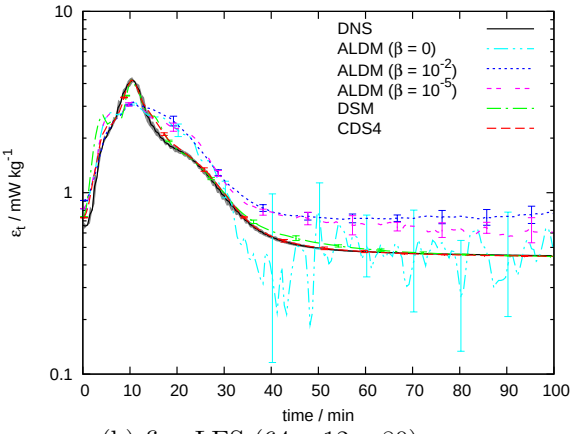

(b) fine LES ($64 \times 12 \times 80$): ε_t

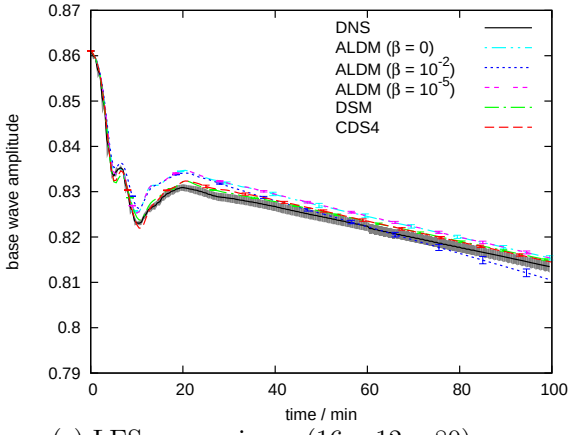

(c) LES, coarse in $x_\parallel$ ($16 \times 12 \times 80$): a

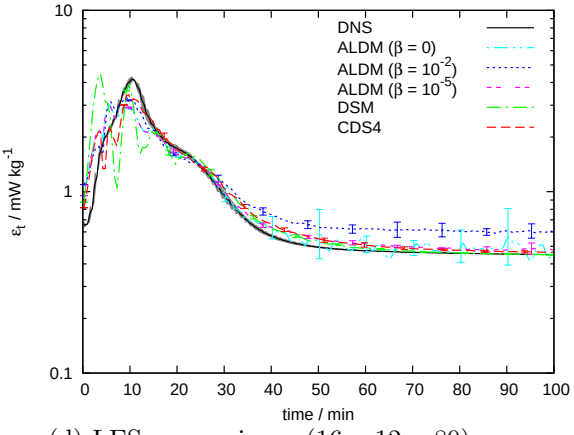

(d) LES, coarse in $x_\parallel$ ($16 \times 12 \times 80$): ε_t

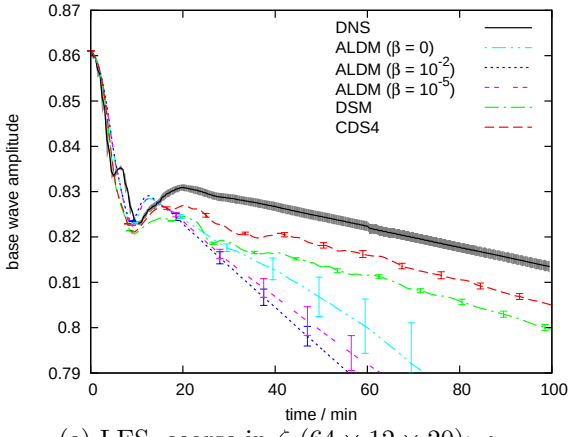

(e) LES, coarse in ζ ($64 \times 12 \times 20$): a

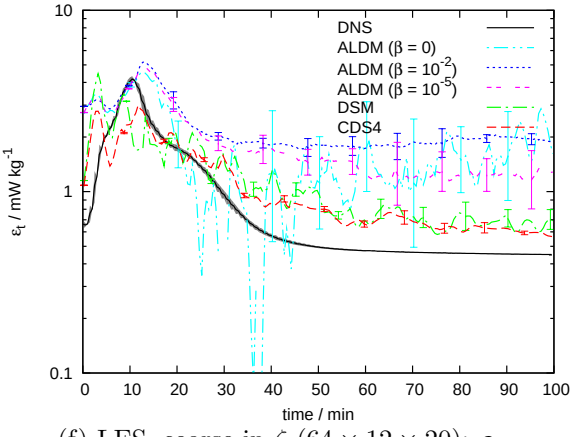

(f) LES, coarse in ζ ($64 \times 12 \times 20$): ε_t

FIG. 8. Statically stable IGW (3-D): Base wave amplitude a and total dissipation rate ε_t at three different LES resolutions. The grey shaded area indicates the standard deviation of five DNS and the error bars indicate the standard deviation of nine LES.

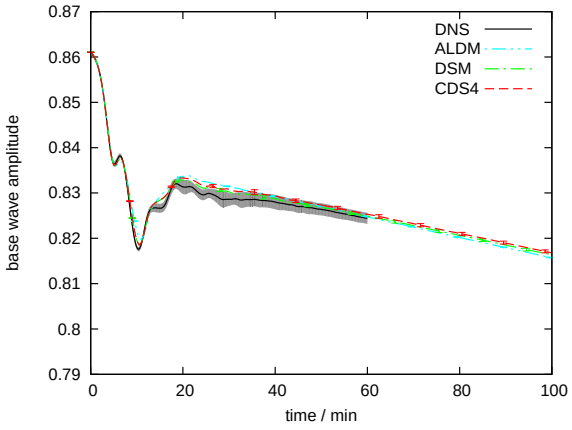

(a) fine LES (64×80): a

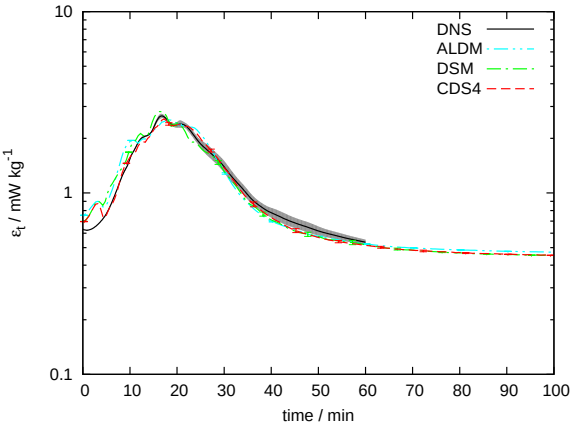

(b) fine LES (64×80): ε_t

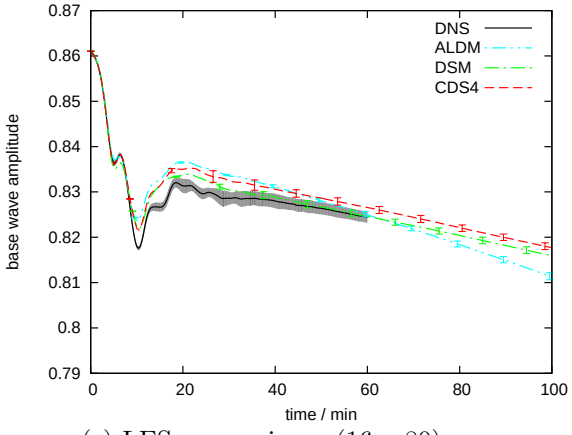

(c) LES, coarse in $x_\parallel$ (16×80): a

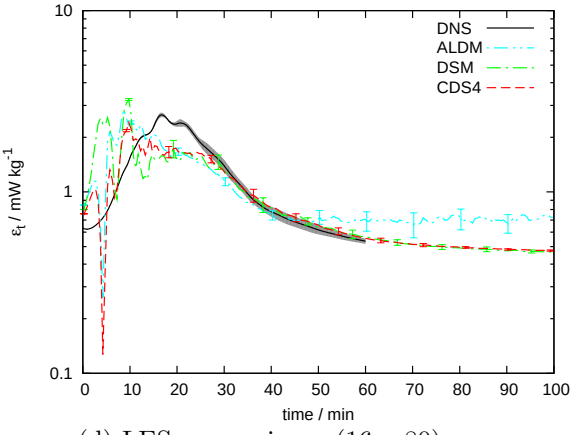

(d) LES, coarse in $x_\parallel$ (16×80): ε_t

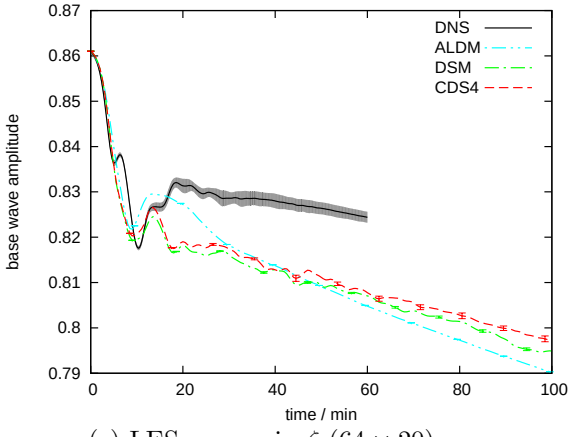

(e) LES, coarse in ζ (64×20): a

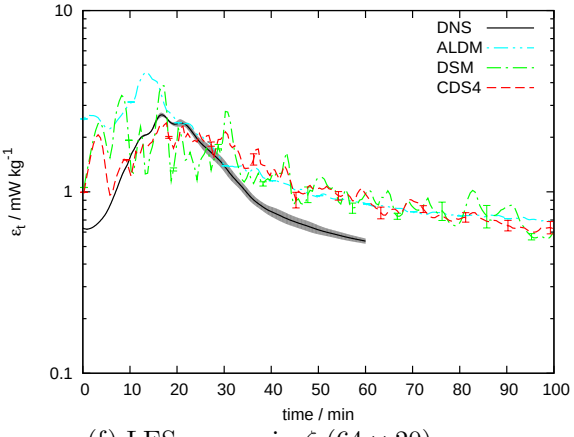

(f) LES, coarse in ζ (64×20): ε_t

FIG. 9. Statically stable IGW (2.5-D): Base wave amplitude a and total dissipation rate ε_t at three different LES resolutions compared with a and resolved dissipation rate ε_m from DNS. The grey shaded area indicates the standard deviation of six DNS, the error bars indicate the standard deviation of nine LES.

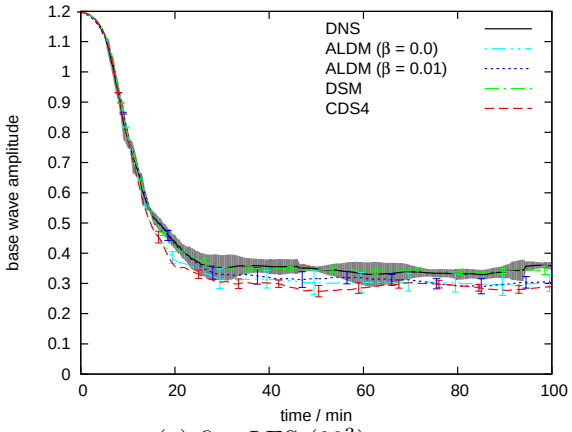

(a) fine LES (80^3): a

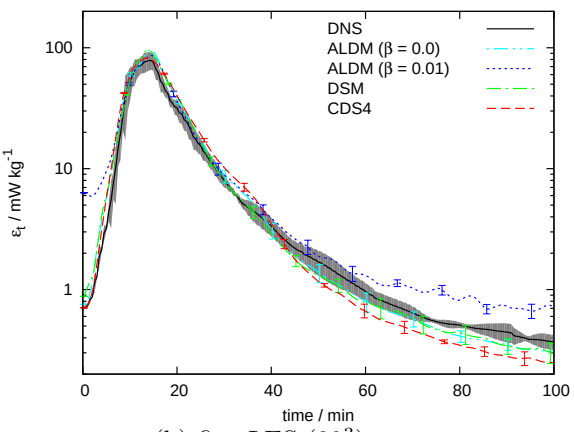

(b) fine LES (80^3): ε_t

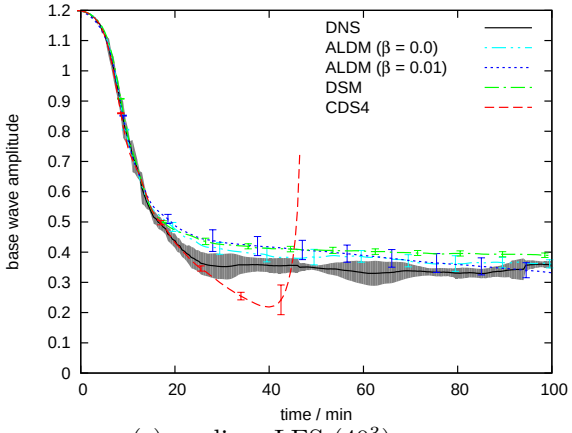

(c) medium LES (40^3): a

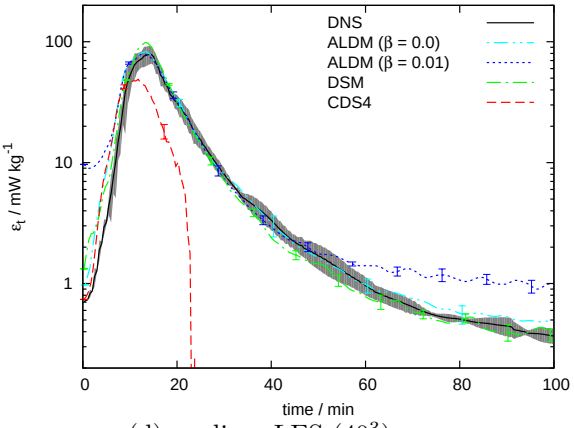

(d) medium LES (40^3): ε_t

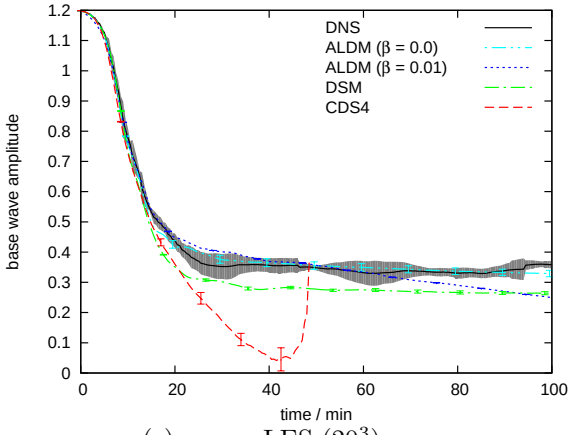

(e) coarse LES (20^3): a

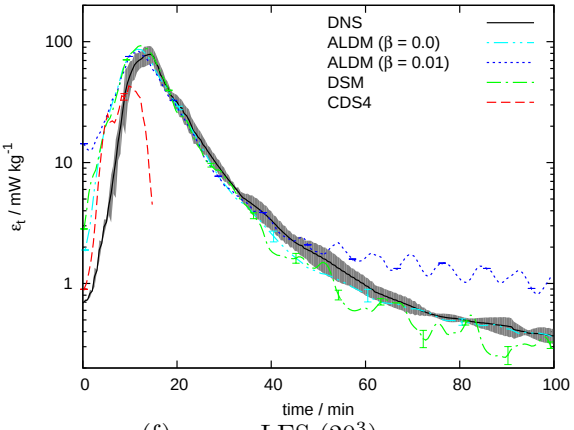

(f) coarse LES (20^3): ε_t

FIG. 10. Statically unstable HGW (3-D): Base wave amplitude a and total dissipation rate ε_t at coarse, medium and fine LES resolution. The grey shaded area indicates the standard deviation of five DNS, the error bars indicate the standard deviation of nine LES.

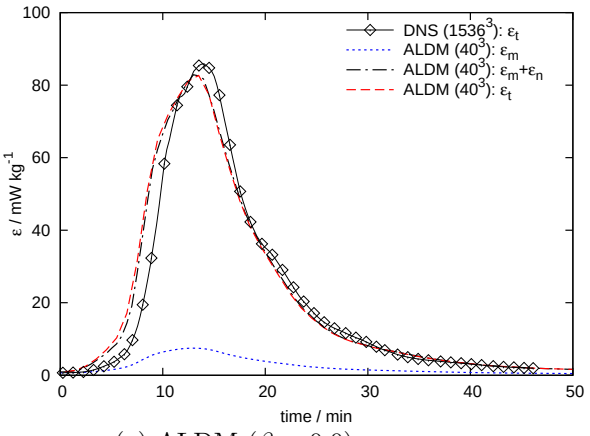

(a) ALDM ($\beta = 0.0$): ε_{m}, ε_{n}, ε_{t}

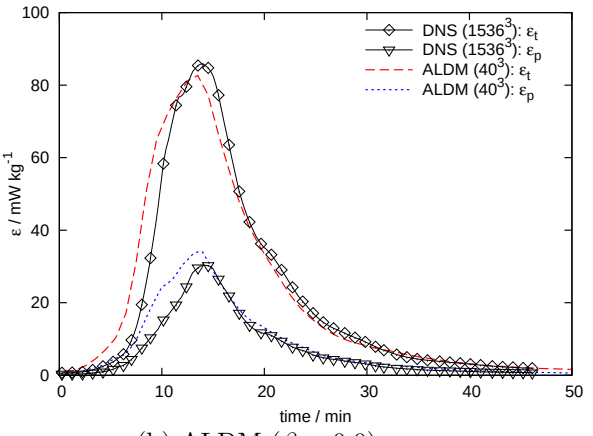

(b) ALDM ($\beta = 0.0$): ε_{p}, ε_{t}

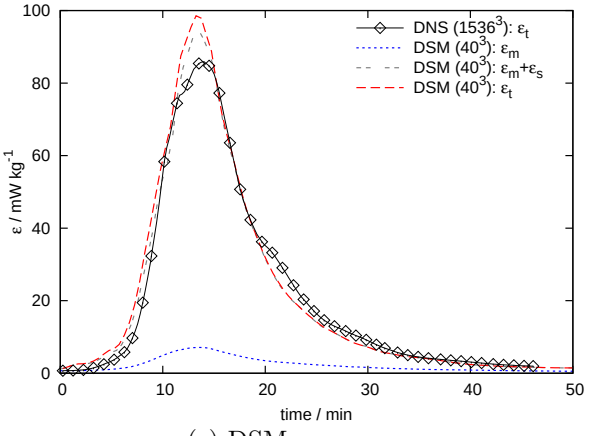

(c) DSM: ε_{m}, ε_{s}, ε_{t}

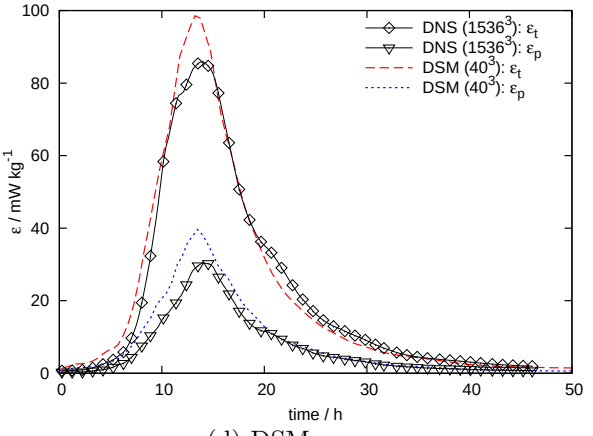

(d) DSM: ε_{p}, ε_{t}

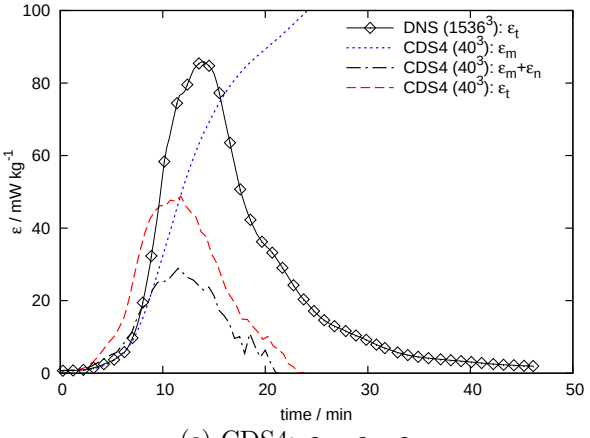

(e) CDS4: ε_{m}, ε_{n}, ε_{t}

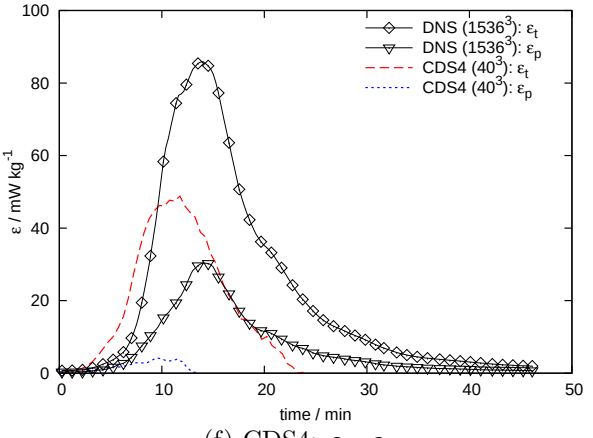

(f) CDS4: ε_{p}, ε_{t}

FIG. 11. Statically unstable HGW (3-D): Comparison of resolved (ε_{m}), numerical (ε_{n}), parametrised (ε_{s}) and total (ε_{t}) dissipation (left column) and thermal (ε_{p}) and total dissipation (right column) during the first breaking event (DNS: single simulation, LES: ensemble averages).

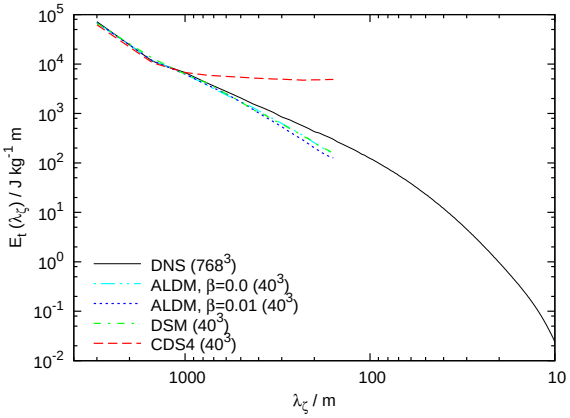

(a) E_t at max. dissipation ($t = 15\,\mathrm{min}$)

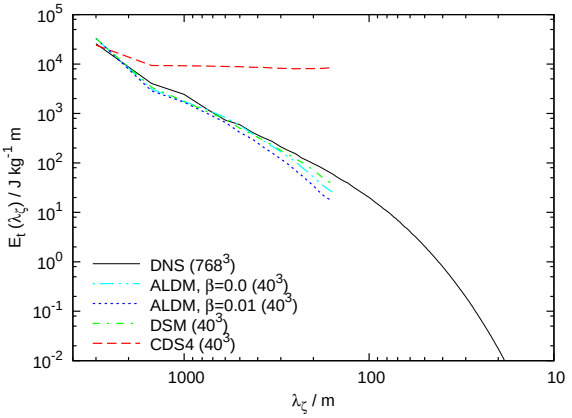

(b) E_t at $t = 30\,\mathrm{min}$

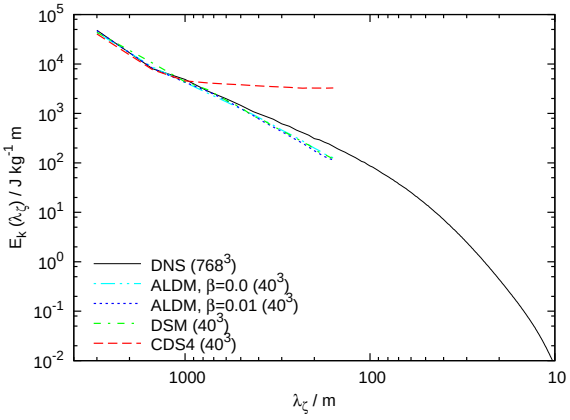

(c) E_k at max. dissipation ($t = 15\,\mathrm{min}$)

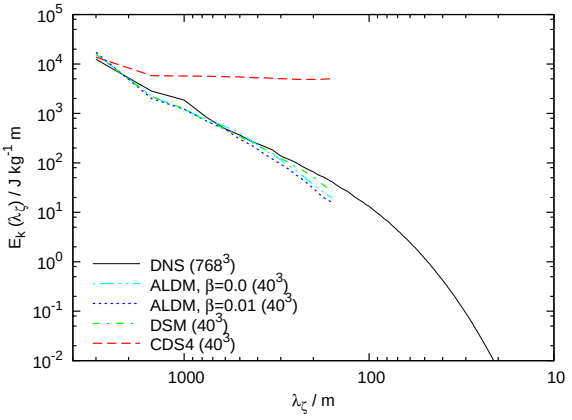

(d) E_k at $t = 30\,\mathrm{min}$

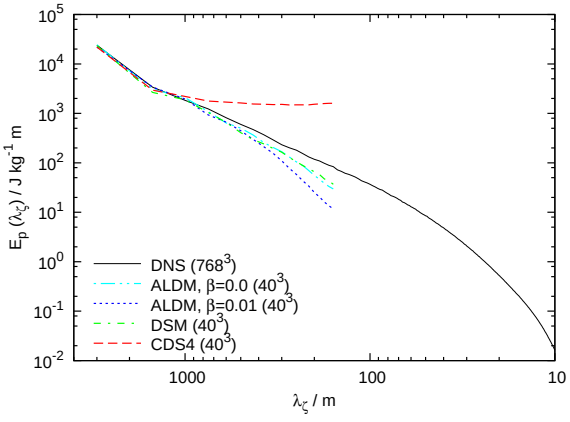

(e) E_p at max. dissipation ($t = 15\,\mathrm{min}$)

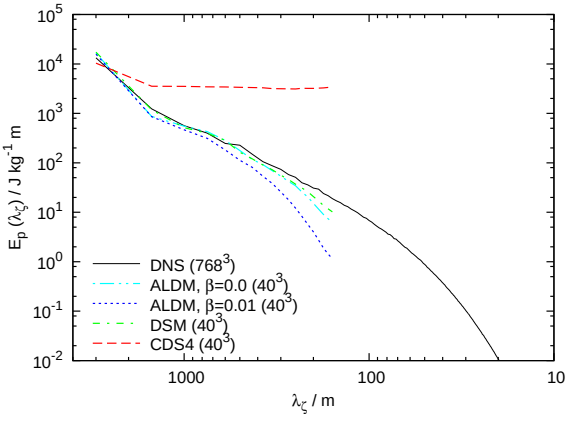

(f) E_p at $t = 30\,\mathrm{min}$

FIG. 12. Statically unstable HGW (3-D): Distributions of total, kinetic and potential energy over vertical wavelength λ_ζ at the moment of maximum total energy dissipation (left column) and at $t = 30\,\mathrm{min}$ (right column) (DNS: single simulation, LES: ensemble averages).

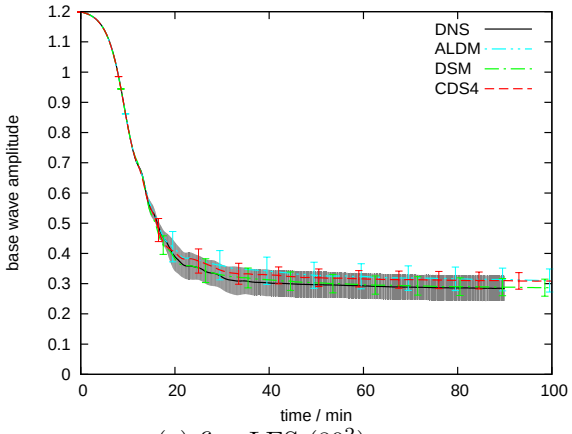

(a) fine LES (80^2): a

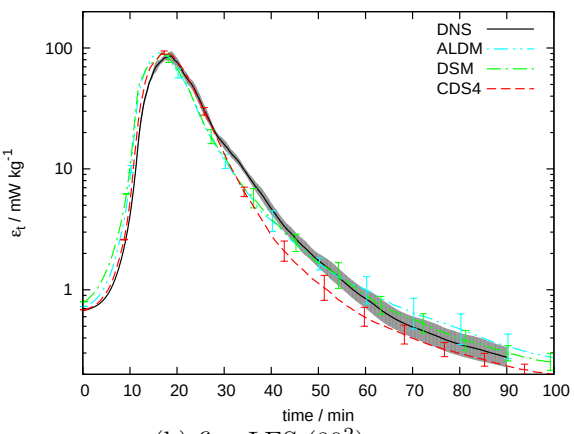

(b) fine LES (80^2): ε_t

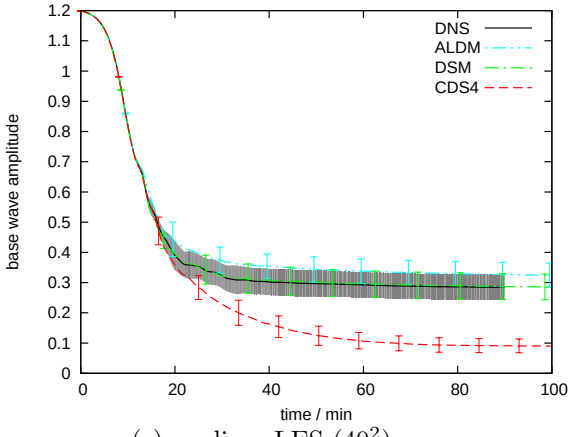

(c) medium LES (40^2): a

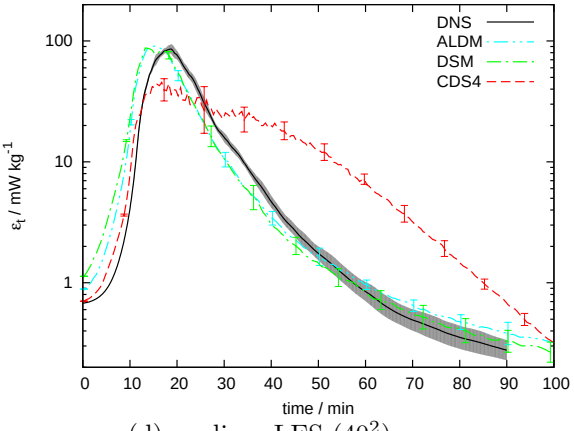

(d) medium LES (40^2): ε_t

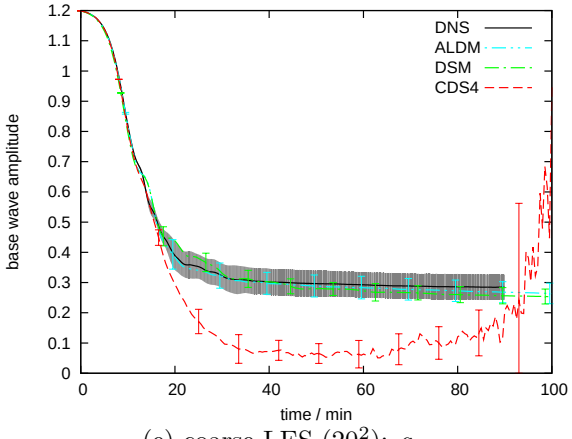

(e) coarse LES (20^2): a

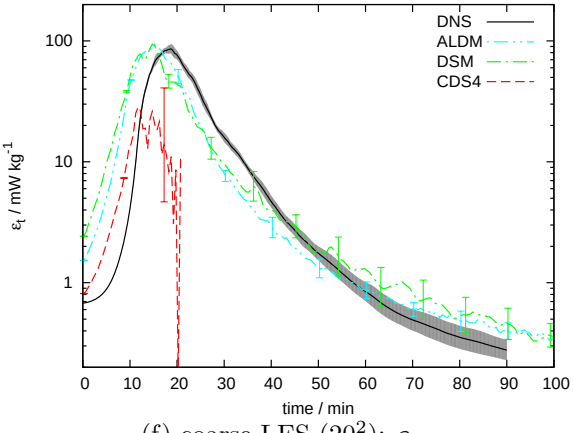

(f) coarse LES (20^2): ε_t

FIG. 13. Statically unstable HGW (2.5-D): Base wave amplitude a and total dissipation rate ε_t at coarse, medium and fine LES resolution compared with a and resolved dissipation rate ε_m from DNS. The grey shaded area indicates the standard deviation of six DNS, the error bars indicate the standard deviation of nine LES.